How Hot Is Too Hot? Disentangling Mid-Cretaceous Hothouse Paleoclimate from Diagenesis

A. C. Fetrow[1]*, K. E. Snell[1], R. V. Di Fiori[2], S. P. Long[3], and J. W. Bonde[4]

[1] University of Colorado Boulder, Boulder, CO, USA. [2] Idaho Geological Survey, University of Idaho, Moscow, ID, USA. [3] Washington State University, Pullman, WA, USA. [4] Nevada Science Center, Henderson, NV, USA.

*Corresponding author: A. C. Fetrow (anne.fetrow@colorado.edu)

Key Points:

- Deeper palustrine and unaltered lacustrine carbonates record warm season water temperatures of approximately 41°C and 38°C, respectively.
- High temperatures from well-preserved shallower palustrine carbonates likely reflect radiative heating.
- Careful facies analysis is imperative for robust paleoclimate interpretation of heterogeneous terrestrial carbonate archives.

Abstract

The North American Newark Canyon Formation (~113–98 Ma) presents an opportunity to examine how various terrestrial carbonate facies reflect different aspects of paleoclimate during one of the hottest periods of Earth's history. We combined carbonate facies analysis with ^{13}C, ^{18}O, and Δ_{47} datasets to assess which palustrine and lacustrine facies preserve stable isotope signals that are most representative of climatic conditions. Type section palustrine facies record the heterogeneity of the original palustrine environment in which they formed. Using the pelmicrite facies that formed in deeper wetlands, we interpret a lower temperature zone (35–40°C) to reflect warm season water temperatures. In contrast, the mottled micrite facies reflects hotter temperatures (36–68°C). These hotter temperatures preserve radiatively heated "bare-skin" temperatures that occurred in a shallow depositional setting. The lower lacustrine unit has been secondarily altered by hydrothermal fluids while the upper lacustrine unit likely preserves primary temperatures and $^{18}O_{water}$ of catchment-integrated precipitation. Based on this investigation, the palustrine pelmicrite and lacustrine micrite are the facies most likely to reflect ambient climate conditions, and therefore, are the best facies to use for paleoclimate interpretations. Average warm season water temperatures of 41.1±3.6°C and 37.8±2.5°C are preserved by the palustrine pelmicrite (~113–112 Ma) and lacustrine micrite (~112–103 Ma), respectively. These data support previous interpretations of the mid-Cretaceous as a hothouse climate. Our study demonstrates the importance of characterizing facies for identifying the data most representative of past climates.

Plain Language Summary

Considered a "supergreenhouse" world, the Cretaceous (145-65 million years ago) was one of the hottest periods in geologic history. Understanding how environments respond to extreme global warmth provides insights that will help to mitigate the harmful effects of modern climate change. Geochemical signals, like stable isotopes, preserved in rocks allow us to reconstruct past climate conditions. We use stable isotope geochemistry on limestones (rocks made of carbonate minerals) to estimate average mid-Cretaceous (~110 Mya) summer temperatures in Nevada, USA. We examine limestones that formed in wetlands and lakes to assess which types record signals representative of the original landscape and which have values that were altered after the rock formed. We find that carbonates deposited in the shallowest parts of wetland environments record temperatures much hotter than air or deeper water temperatures due to extreme land surface heating, while deeper wetland limestones preserve temperatures more representative of ambient conditions. Average warm season water temperatures for wetland and lake carbonates are approximately 41°C and 38°C, respectively, revealing hot conditions during the Cretaceous that support our understanding of the Cretaceous as a greenhouse world. This research provides an example of how to interpret useful climate information from complex carbonate datasets.

1 Introduction

The Cretaceous was a time of highly active tectonism, including the ongoing breakup of supercontinent Pangaea and increased seafloor spreading rates, as well as of greenhouse climate, including elevated global temperatures and a reduced equator-to-poles temperature gradient (Forster et al., 2007; Huber et al., 2002; Huber, 2008; Pagani et al., 2013; Takashima et al., 2006). The mid-Cretaceous (~113–89 Ma) marks particular warmth, evolving from a "warm greenhouse" to a "hot greenhouse," during the Cretaceous Thermal Maximum (~95–90 Ma) (Forster et al., 2007; Huber et al., 2018). Much more is known about the response of marine environments during this time than terrestrial environments. Terrestrial carbonates offer potential archives through which to examine the past climatic, hydrologic, environmental, and surface elevation conditions using a variety of proxy tools, such as stable isotopes (i.e., ^{13}C, ^{18}O, and Δ_{47}). Lacustrine and pedogenic carbonates, have been used extensively as paleoclimate archives (e.g., Gierlowski-Kordesch, 2010; Ingalls et al., 2022; Passey et al., 2010; Petersen et al., 2019; Quade et al., 2013; Snell et al., 2013), while palustrine (i.e., wetland) carbonates have not. Palustrine environments represents a depositional spectrum between open water (i.e., lacustrine) and subaerially exposed (i.e., pedogenic) portions of the landscape (Alonso-Zarza, 2003; Alonso-Zarza & Wright, 2010b; Arenas-Abad et al., 2010a). Palustrine rocks exhibit characteristics of both ends of the depositional spectrum, and their complex mixture of sedimentary processes demands that they be considered a distinctive depositional setting from lacustrine and pedogenic environments. Therefore, to understand how past terrestrial environments respond spatially and temporally to different climate states, we must understand how these archives encode environmental signals differently and consider the heterogeneity that exists within the same depositional system and/or proxy archive.

We studied the sedimentology and stable isotope geochemistry of the North American Newark Canyon Formation (NCF; ~113–98 Ma) to better understand how continental interiors responded to the globally hot conditions of the mid-Cretaceous, and to improve our understanding of how palustrine and lacustrine environments capture paleoclimate and paleoenvironmental signals during a period of unique climatic history. The NCF type section preserves a sequence of palustrine, fluvial, and lacustrine sediments. Using facies analysis, optical and cathodoluminescence (CL) microscopy, X-ray diffraction (XRD), and stable isotope geochemistry ($^{13}C_{carb}$, $^{18}O_{carb}$, $^{18}O_{water}$, and Δ_{47} temperatures (i.e., T($_{47}$)), we assessed which palustrine and lacustrine facies preserve unaltered stable isotope proxy signals that are also most representative of climatic and environmental conditions of the depositional landscape. Finally, we evaluated the paleoclimatic and paleoenvironmental conditions in the Sevier Hinterland region of southwestern North America during the mid-Cretaceous (Figure 1).

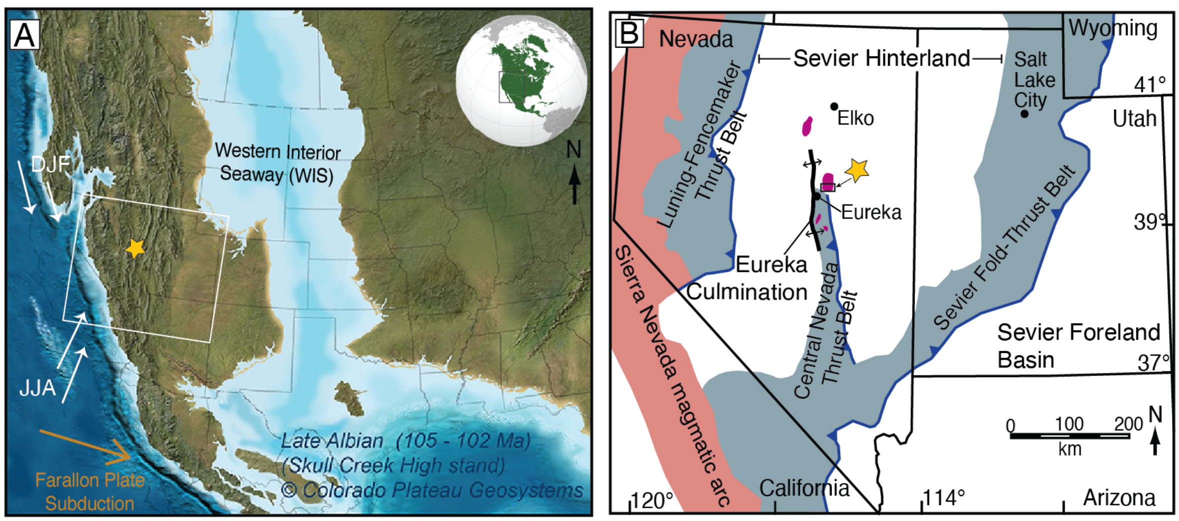

Figure 1. Yellow star in both maps represents the approximate site of deposition of the NCF type section. a) Reconstruction map of southern North American during the late Albian (~105 to 102 Ma; modified from Blakey, 2020). Modeled seasonal prevailing wind directions are shown for Albian (~100 Ma) winter (DJF: December, January, February) and summer (JJA: June, July, August) months with white arrows (Elder, 1988; Poulsen et al., 1999). Dark orange arrow shows approximate direction of subduction of the Farallon plate (DeCelles, 2004; DeCelles & Graham, 2015). The white box indicates the area of the map shown in b) Regional tectonic map adapted from Di Fiori et al. (2020) and Long et al. (2014). Gray shading shows the approximate spatial extents of Jurassic-Cretaceous deformational provinces of the North American Cordilleran mountain belt in western United States, while pink shading marks the Sierra Nevada magmatic arc (from Van Buer et al. (2009)). All mapped NCF depositional basins are shown in purple (from Di Fiori et al., 2021).

2 Background

2.1 Overview of Cretaceous climate

2.1.1 Cretaceous temperature records

During the Cretaceous, estimates of globally averaged surface temperatures suggest climate was 6–12ºC warmer than pre-industrial (Barron, 1983; Barron et al., 1993; Barron & Washington, 1982; Gale, 2000; Huber et al., 2002), with a reduced equator-to-poles temperature gradient that was likely caused by a combination of changes in land-sea distributions, elevated atmospheric concentration of CO_2, increased efficiency of atmospheric and oceanic heat transport, and/or changes in oceanic deep water production (Barron et al., 1993; Barron & Washington, 1982, 1984; Huber et al., 1995; Poulsen et al., 1999; Ludvigson et al., 2015). During the mid-Cretaceous, defined here as ~113 to 89 Ma (start of the Albian stage to the end of the Turonian stage), global climate evolved from a "warm greenhouse" to a "hot greenhouse" at the Cretaceous Thermal Maximum where it reached apex of warmth during the early to mid-Turonian (Forster et al., 2007; Huber et al., 2018). There is little evidence of any permanent ice during the mid-Cretaceous apart from a few studies that speculate that for latitudes greater than 75ºS there were cool temperate regional climates and the potential development of small ice sheets (Frakes & Francis, 1988; Miller et al., 2003; Rich et al., 1988). Foraminiferal $^{18}O_{carb}$ values from southern high latitudes shows that there were warm conditions throughout the Albian (~113–100 Ma) followed by extreme warmth during the mid-Turonian (~91 Ma) (Huber et al., 2018). ^{18}O data from brachiopods from northern European indicate that temperatures in the mid-latitudes rose 6–7°C during the latest Cenomanian, reached a maximum at the Cenomanian-Turonian boundary (93 Ma), and continued into the mid-Turonian (Jenkyns, 2010; Voigt et al., 2006).

On land, frost-intolerant vertebrate and plant assemblages suggest that mean annual temperatures at polar latitudes were much warmer than today in both hemispheres during the Cretaceous, with winter temperatures above freezing (Brouwers et al., 1987; Case et al., 2000; Olivero et al., 1991; Parrish et al., 1987; Parrish & Spicer, 1988; Rich et al., 2002; Tarduno et al., 1998). Seasonal range of temperature may have been drastically reduced during the Cenomanian at mid-latitudes due to major paleogeographic events, such as the dislocation of Gondwana in the southern hemisphere and flooding of North America, Africa, and Eurasia Fluteau et al. (2007). North American mid-latitude sites preserve elevated mean annual and mean warm season temperatures during the mid-Cretaceous across paleolatitudes (Gröcke et al., 1999; Ludvigson et al., 2010, 2015; Suarez et al., 2014; Suarez et al., 2021).

2.1.2 Invigorated hydrologic cycle

Cretaceous climate is hypothesized to have had an invigorated hydrologic cycle, which means that areas of high precipitation became wetter and arid areas became drier (Barron & Washington, 1982; Held & Soden, 2002, 2006; Ufnar et al., 2004). Based on the spatio-temporal distribution of deserts and modeled prevailing wind directions, an equatorward contraction in the Hadley circulation during the mid-Cretaceous is speculated to have created a belt of increased humidity in the mid-latitudes (Hasegawa et al., 2012; Qiao et al., 2022). During the more humid periods of the Cretaceous, intensified greenhouse conditions developed because of the increased latent heat capacity of the atmosphere. This, in turn, may have further invigorated the hydrologic cycle, leading to intensifying precipitation events and increased tropical cyclone and monsoonal activity in some regions (Poulsen et al., 2001; Suarez et al., 2011; White et al., 2001). This invigoration of the hydrologic cycle would have particularly effected mid-latitude continental interiors, and would have caused changes in erosion rates and the timing and frequency of erosional events (Barron et al., 1989; Burgener et al., 2019; Suarez et al., 2011). It has been proposed that as a result of the intensified hydrologic cycle, humid climate belts during the mid-Cretaceous were larger than those of the present day (Barron & Washington, 1982; Föllmi, 2012; Hay et al., 2018). Additionally, facilitated by the presence of numerous, km-scale rift systems caused by the continued breakup of the Pangea supercontinent, humid conditions likely increased the volume of water stored in groundwater reservoirs and terrestrial water bodies (e.g., lakes and wetland systems) (Föllmi, 2012; Hay et al., 2018; Wendler & Wendler, 2016). In the western US, paleo-precipitation reconstructions from Albian-Cenomanian vertic paleosol profiles suggest that climate at ~30ºN paleolatitude site in north-central Texas and southern Oklahoma during the Cretaceous was similar to modern tropical climates (Andrzejewski & Tabor, 2020). Additionally, stable isotope mass-balance modeling of meteoric ^{18}O values from North American paleosol siderites from the Cenomanian show that precipitation rates were significantly higher than present day for mid-latitude sites (40–60ºN) (Albian: 2200 mm/yr at 45°N; Cenomanian: 3600 mm/yr at 45°N) (Ufnar et al., 2008). Finally, the Cedar Mountain Formation rocks yielded paleo-precipitation estimates of 735 to 1042 mm/yr (Suarez et al., 2021).

2.2 Geologic background of the Newark Canyon Formation

2.2.1 Tectonic setting of the western United States in the Mesozoic

Subduction of oceanic plates of the Pacific realm under the western margin of the North American continental plate took place from the Jurassic to the Paleogene, giving rise to contractional deformation that thickened the crust, and built the vast North American Cordilleran mountain belt (Burchfiel et al., 1992; DeCelles, 2004; DeCelles & Coogan, 2006; Dewey & Bird, 1970; Dickinson, 2004; Jordan & Allmendinger, 1986; Yonkee & Weil, 2015). The area where the NCF was deposited is part of the broader Sevier hinterland, which is flanked by the Sierra Nevada magmatic arc to the west and the Sevier fold–thrust belt to the east (Figure 1) (DeCelles, 2004; DeCelles & Coogan, 2006; Long et al., 2014; Wells et al., 2012). Locally, the structures associated with the NCF are part of the Central Nevada Thrust belt, with a structural high known as the Eureka Culmination in the area adjacent to the NCF type section.

2.2.2 Age of the Newark Canyon Formation type section

The NCF type section unconformably overlies either the Permian Carbon Ridge Formation, which is composed of marine shelf carbonates, siltstones, conglomerates, or the Mississippian shallow marine Ely Limestone (Druschke et al., 2011; Nolan et al., 1956; Nolan & Hunt, 1962; Strawson, 1981; Vandervoort, 1987). The NCF is unconformably overlain by Paleogene volcanics and megabreccias. Based on the presence of Early Cretaceous freshwater unionids, gastropods, ostracods, and fish fossils, and charophytes and other plant macrofossils, the depositional age of the NCF type section exposure was originally estimated to be Aptian–Albian (ca. 126 to 100 Ma) (David, 1941; Fouch et al., 1979; MacNeil, 1939; Nolan et al., 1956; Smith & Ketner, 1976). Recently, the faunal list from NCF exposures across central Nevada has expanded to include a turtle genus Glyptops, a member of the freshwater shark family Hybodontidae, a gar fish (Lepisosteidae), two types of crocodilians, and a number of dinosaur families, and is interpreted as Early Cretaceous based on this faunal assemblage (Bonde et al., 2015). U-Pb zircon geochronology from a water-lain tuff yielded a concordia age of a coherent population of zircons at 103.0 ± 0.7 Ma for the top of the NCF type section (Figure 2) (Di Fiori et al., 2020). Additionally, U-Pb geochronology of detrital zircons yielded maximum depositional age (MDA) estimates for different units of the type section of 113.7 ± 2.3 Ma, 112.92 ± 1.0 Ma, and 98.6 ± 1.9 Ma (Fetrow et al., 2020; Di Fiori et al., 2020). The 113.7 ± 2.3 Ma MDA was from a basal mudstone sample located ~ 10 km north of the type section, in the Hildebrand exposure of the NCF (Di Fiori et al., 2020).

2.2.3 Deposition of the Newark Canyon Formation

The NCF was deposited in a series of spatially-isolated piggyback basins that are distributed along a narrow, ~150 km-long, N-S-trending region of central Nevada following the Central Nevada thrust belt (Figure 1) (Di Fiori et al., 2021; Long et al., 2014; Nolan et al., 1956, 1974; Nolan & Hunt, 1962). Deposition in the NCF type section basin is attributed to erosion of the eastern flank of the Eureka Culmination (Figure 1), which is supported by paleo-flow directions from clast orientations and crossbedding from the NCF type section that indicate an east-flowing fluvial system (Di Fiori et al., 2020, 2021; Long 2012, 2015; Long et al., 2014, 2015; Fetrow et al., 2020; Vandervoort & Schmitt, 1990). Di Fiori et al. (2020) divide the NCF type section exposure into five units (Knc1– Knc5). These units stack conformably except for two notable exceptions. First, there is a set of progressive unconformities within Knc3 conglomerate beds where relatively shallow-dipping beds (~17°W) overlie steep-dipping beds (~40°W). Second, there is an angular unconformity at the base of Knc5 that represents ~10 Myr of non-deposition/erosion between Knc4 and Knc5 (Di Fiori et al., 2020).

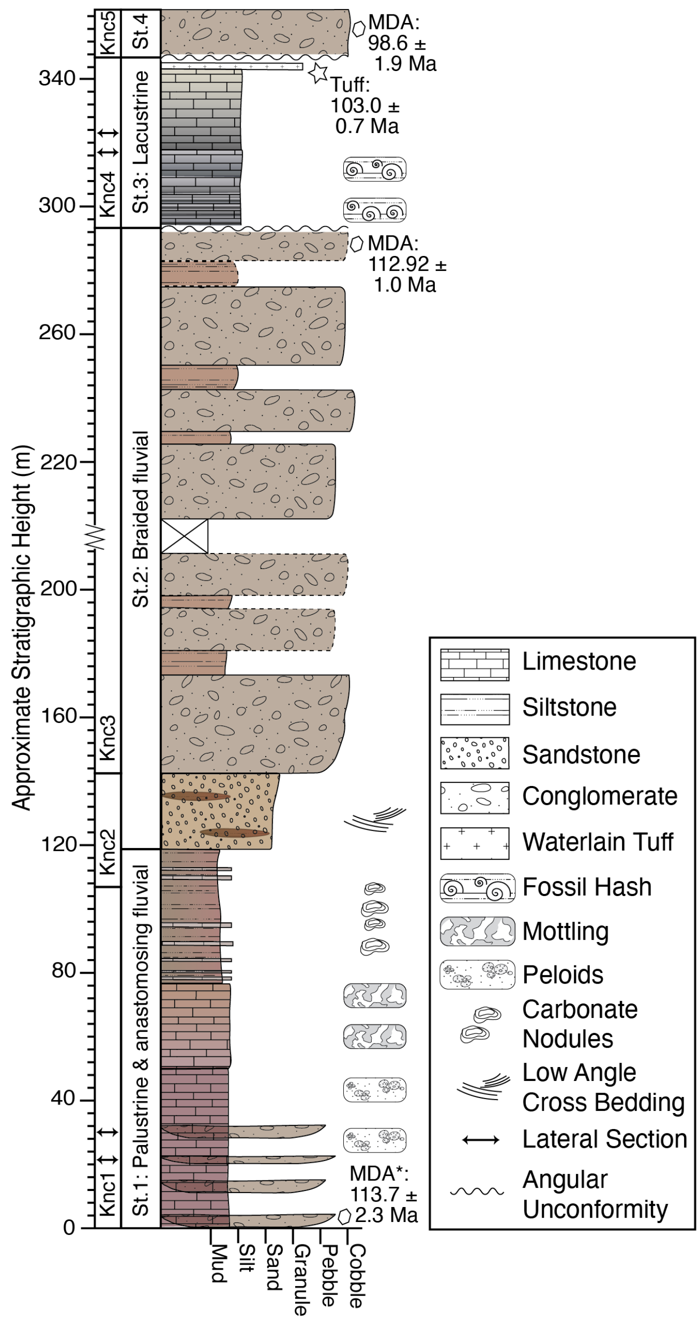

Figure 2. Composite stratigraphic column (meters) of the NCF type section with published age constraints (Di Fiori et al., 2020), integrating stratigraphic and lithologic information from the five measured sections to show general basin

architecture. Samples were assigned stratigraphic heights from this composite stratigraphic column. The four small double-ended arrows indicate the stratigraphic heights of the lateral sections that were measured (21.5, 30, 317, and 323 m). There is an angular unconformity between the lacustrine unit (Knc4, Stage 3) and the capping conglomerate (Knc5, Stage 4). A U-Pb depositional age from a water-lain tuff (star) and three maximum depositional ages (MDAs) from detrital zircons (hexagons) are shown to the right of the stratigraphic column (Di Fiori et al. 2020). *Note: the MDA used for the base of the section is from a basal mudstone sample located 10 km north of the type section.

An in-depth explanation of the facies preserved in the NCF is presented in Fetrow et al. (2020) (for addition key details and representative images, refer to the supplemental materials). The abbreviation convention used in this study first denotes the rock type using the Folk classification system (Folk, 1959, 1962), and then the interpreted depositional environment is given in the subscript. Here we summarize the key deposition environments and associated facies. Knc1-Kn5 correspond to four depositional stages (Stage 1–4 of Fetrow et al. 2020) (Figure 2). Stage 1 was dominated by deposition within an anastomosing river floodplain where active channels were separated by interchannel topographic lows in which heterogeneous, seasonally ephemeral palustrine environments formed (Figure 3). Depending on proximity to active channels, these wetland environments experienced variable frequencies and quantities of inundation and input of siliciclastic clast material (pebbly conglomerate facies, $\mathrm{Gc}_{\mathrm{(channel)}}$). Because of these highly variable flooding events, different portions of the wetlands experienced a spectrum of water depths, represented by different facies: areas that likely remained fully submerged (pebbly pelmicrite facies, $\mathrm{Mp}_{\mathrm{(wetland)}}$), to shallow water areas that experienced more frequent subaerial exposure and desiccation (mottled micrite facies, $\mathrm{Mm}_{\mathrm{(wetland)}}$), to areas that may have experienced long-duration subaerial exposure that allowed for well-developed pedogenesis (carbonate nodule-bearing paleosol facies, $\mathrm{Mn}_{\mathrm{(soil)}}$). Farther from the active anastomosing channels, and therefore subject to less frequent inundation events, ponds formed in abandoned channels and slowly filled with allochthonous siliciclastic and autochthonous carbonate sediment (pond biomicrite facies, $\mathrm{Mb}_{\mathrm{(pond)}}$). These infilled ponds in the channel-distal portions of the river plain underwent minimal weak pedogenesis (e.g., paleosol facies). The highly variable conditions of the anastomosing river system caused frequent lateral facies shifts that created complex vertical arrangements of these facies within Stage 1 of the type section.

A braided river system dominated deposition during Stage 2, preserving bedded pebbly to cobble conglomerates and planar-bedded sandstones, and was likely caused by an increase in structural uplift along the nearby Eureka Culmination that increased sediment supply and the fluvial gradient in the NCF basin (Fetrow et al., 2020). Stage 2 does not preserve any carbonate-bearing facies. Stage 3 was marked by a large-scale, freshwater, balance-filled lacustrine system that indicates either a reorganization of drainage patterns due to new structural containment or an increase in accommodation potentially due to subsidence in the piggyback basin while the sediment supply remained relatively constant (Fetrow et al., 2020). Lacustrine mudstones (calcareous mudstone facies, $Fc_{(lake)}$), biomicrites containing abundant fossil hash (biomicrite, $Mb_{(lake)}$), and non-fossiliferous micrite (micrite facies, $M_{(lake)}$) are preserved in Stage 3. After either a depositional hiatus or extensive erosion representing ~10 Myr, Stage 4 suggests a likely reinitiation of deformation in the region, represented by deposition of the final capping pebble to cobble conglomerate (Fetrow et al., 2020).

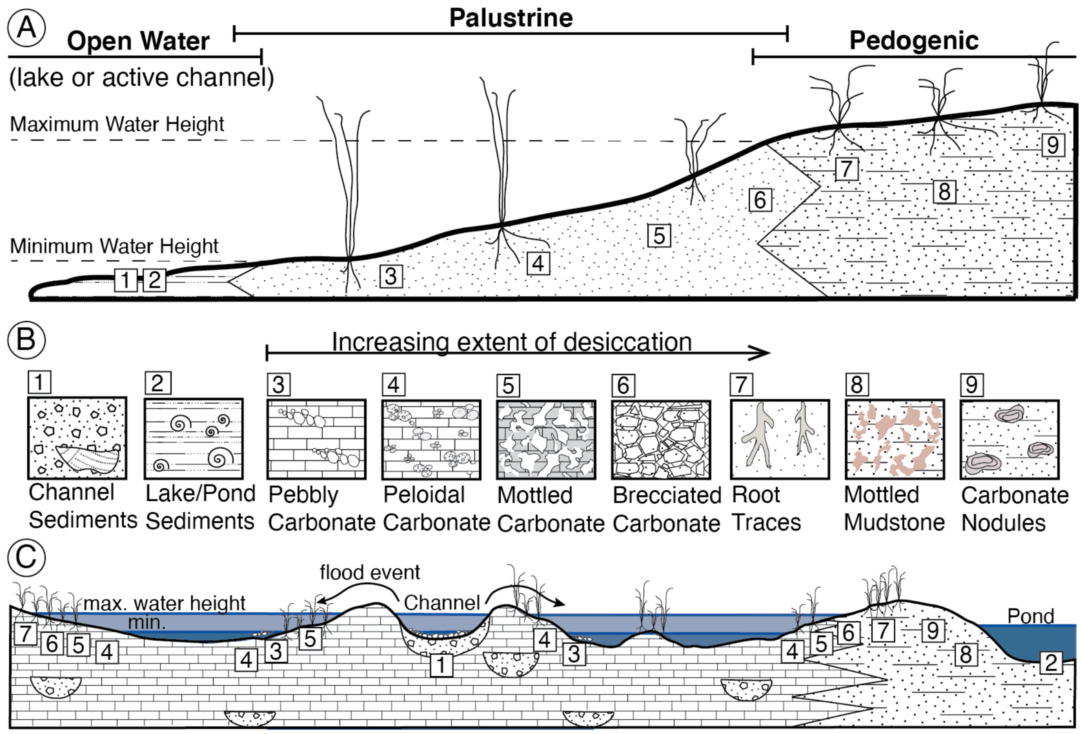

Figure 3. a) Generalized cross section depositional model for a palustrine environment that spans across open water (e.g., a pond/lake or active fluvial channel) through a palustrine transitional zone to a pedogenic system (modified from Alonso-Zarza, 2003). The fluctuation of surface water in the palustrine zone between a minimum and maximum height creates a spectrum of heterogeneous depositional features. b) Numbers refer to a spectrum of common depositional features and textures found in carbonate-bearing systems. Some portions of the landscape remain subaqueous while others experience periodic oscillations in the height of surface water, and therefore, are subject to heterogeneous quantities and extents of desiccation, reworking, and overprinting by pedogenic processes. c) Depositional model for the palustrine facies preserved in Stage 1 of the Newark Canyon Formation type section. Numbers refer to panel

B and provide examples of where depositional features and facies can form along the palustrine landscape. Periodic inundations created a highly variable palustrine system between active river channels.

2.3 Seasonal biases of terrestrial carbonate records

To use terrestrial carbonate archives for paleoclimate interpretations, it is important to account for when in the year carbonates form, and therefore, identify to which season(s) their paleotemperature records correspond. The timing and extent of carbonate formation across depositional settings is the product of a combination of environmental factors that can include temperature, timing and style of precipitation, substrate texture and pH, presence or absence of vegetation, and concentration of major cation (e.g., Ca^{2+}, Mg^{2+}) and carbonate anions (i.e., HCO_3^- and CO_3^{2-}) (e.g., Breecker et al., 2009; Burgener et al., 2018; Huntington et al., 2010; Ingalls et al., 2020; Zamanian et al., 2016). While not much is known about palustrine carbonate formation, we can use lakes and soil carbonates as guides because palustrine environments exist on a gradient between these two environments. There is growing body of evidence that suggests that formation of soil carbonate nodules is principally controlled by increased carbonate saturation state due to enhanced transport of Ca^{2+} from the surface into the soil column and evaporative concentration of Ca^{2+} and CO_3^{2-} ions in soil water that occurs during dry-down periods (Breecker et al., 2009; Burgener et al., 2016, 2018; Gallagher & Sheldon, 2016). These periods of significant wetting and drying cycles often correspond to warm seasons where precipitation cycles are more episodic and wetting and drying cycles can be more pronounced (Breecker et al., 2009; Hough et al., 2014; Kelson et al., 2020). Therefore, since pedogenic carbonate formation is found to preferentially occur during warm, episodically dry periods, clumped isotope temperatures may often reflect mean warmest month temperature rather than mean annual temperature (Breecker et al., 2009; Passey et al., 2010; Quade et al., 2013). Similarly, lacustrine carbonates typically preserve warm season bias, although the timing of precipitation in lacustrine settings is also controlled by seasonal mixing, alkalinity, influence of biologic activity, and evaporation (e.g., Huntington et al., 2010; Ingalls et al., 2020). Lacustrine carbonates may preserve cooler temperatures with commonly dampened expression of seasonal variability than palustrine carbonates due to a slower seasonal response of water temperature with increased water depth (Dee et al., 2021). Based on these findings, we expect a similar warm season bias in the formation of carbonate in palustrine environments in the NCF, but this remains an unresolved question since no studies have yet explored Δ_{47} thermometry in palustrine carbonate facies and few have explored $^{13}C_{carb}$ and $^{18}O_{carb}$ systematics.

3 Materials and Methods

3.1 Field and hand sample preparation

We measured and described the stratigraphy of the NCF type section located east of Eureka, Nevada during field sessions in 2016 and 2017 (Figure 1). The field methods and resulting sedimentary interpretation from these field sessions were described in Fetrow et al. (2020). Hand samples (n=208) were collected from all exposed carbonate beds and the presence of carbonate in the samples was assessed in the field by testing for reactivity with dilute hydrochloric acid. We sampled carbonate beds at ~0.5 m increments throughout the vertical measured sections where exposure permitted or where we could dig to reasonable exposure, although due to thick overlying colluvium this was not possible in several intervals.

In addition to sampling up section through stratigraphic height, four "lateral transects" were measured and described, and samples were collected along-strike at four stratigraphic heights (21.5, 30, 317, 323 m) (Figure 2). Two lateral sections were measured in the lower part of the type section (member Knc1; stage 1) to document the lateral heterogeneity of the palustrine depositional landscape at two stratigraphic levels. Two lateral sections were also measured in the upper part of the type section (member Knc4; stage 3) to explore lateral heterogeneity and estimate lateral extent of the paleo-lake at two stratigraphic levels.

Hand samples were cut into billets and polished to expose unweathered faces that were used for making thin sections for petrographic analyses and drilling sample powder. Thin sections (n=69) were made by Spectrum Petrographics, Inc. Samples from which ^{13}C, $^{18}O_{carb}$, and Δ_{47} isotope analyses were measured were assessed for diagenetic changes using optical and cathodoluminescence petrography (see section below, and Fetrow et al., 2020). Carbonate mineralogy was determined by petrographic inspection, and, for a subset of samples, XRD analysis. XRD analyses (n=21) were conducted on a Bruker D8 Advance that uses Cu K-alpha radiation and the spectra were processed using Bruker *Diffrac.eva* software to match unknown spectra to the International Centre for Diffraction Data (ICDD) database of known spectra. Representative samples of each of the different carbonate-bearing facies were the primary targets selected for XRD analysis (Table S1).

To prepare samples for geochemical analyses, a dental drill was used to generate ~30–50 mg of fine powder from each hand sample and then homogenized using a mortar and pestle. All isotope analyses were generated from subsamples of this homogenized powder. If additional sample powder was drilled from a sample, we compared the isotopic values and temperature estimates of the two generations of sample powder and considered them "one sample" only if the values of the two generations fell within 1 standard error (1 s.e.) of one another for all measured isotopes. Where quantities allowed, additional spots were drilled from some hand samples to target secondary spars or regions of variable textures, such as microsparite or sparite, to determine isotopic values and formation temperatures of diagenetic events or fluids that created the secondary spars. Some hand samples were subsampled to explore cm-scale heterogeneity, such as regions of lighter and darker colored micrite, in palustrine and lacustrine carbonate-bearing facies (e.g., sample *AF-NCF-TS2-17-21.5A*). More detailed facies descriptions for the lateral sections measured in the NCF type section can be found in Figure 2 in Fetrow et al. (2020) and in the supplemental information (Figure S4 and S5).

Crystalline spar veins were sub-sampled from two NCF carbonate samples from the lower palustrine unit (Stage 1) at stratigraphic heights of 21.5 and 75.6 m (*21.5D_spar* and *31_spar*) (Figure 2). *21.5D_spar* occurs in a pebbly pelmicrite sample and *31_spar* occurs in a mottled micrite sample. Spar veins were sampled carefully using a dissecting microscope to avoid inclusion of the surrounding matrix. In addition, a hand sample of the underlying Carboniferous Ely Limestone was collected just east of the exposure of the NCF type section along the Newark Canyon Road. The sample of Ely Limestone ("Ely LS") and a spar vein found within the sample ("Ely spar") were analyzed as isotopic reference points to be compared against NCF samples.

3.2 Optical and cathodoluminescence microscopy

We used optical and cathodoluminescence microscopy to identify primary depositional fabrics, as well as diagenetic fabrics that may have resulted from dissolution and/or reprecipitation, recrystallization, and later void-filling cements in samples used for $^{13}C_{carb}$, $^{18}O_{carb}$, and Δ_{47} analyses. Optical and cathodoluminescence (CL) images are shown for representative samples chosen from carbonate facies (Figure S1–S3). Samples with > 3 clumped isotope replicates and low standard error for bulk ^{13}C and $^{18}O_{carb}$ (< 0.02‰ and < 0.03‰, respectively) were used as representative examples of the carbonate-bearing facies for the petrographic image plates. CL microscopy was conducted on a Technosyn Cathode Luminescence Model 8200 Mk II microscope. CL colors from carbonate minerals vary between yellow, orange, and red to dull to nonluminescent according to the spatial distribution of trace elements (i.e., Fe and Mn) in carbonate fabrics and the mineralogy (Pagel et al., 2000). CL imaging can be used as a visual aid in determining generations of crystallization through crosscutting relationships and to yield useful information about primary and diagenetic components of carbonate facies (Dunagan & Driese, 1999; Mintz et al., 2011; Wright & Peeters, 1989).

3.3 Stable single carbon and oxygen isotopes (^{13}C and $^{18}O_{carb}$) analytical procedure

Approximately 110–250 µg of sample powder (equivalent to ~100–110 µg of pure carbonate mineral) was weighed into Labco Exetainers vials (12 ml) and purged with ultra-high purity He for 5 minutes. Samples were digested in 105-110% orthophosphoric acid at 70ºC for >30 minutes to release CO_2 for analysis. A linear regression between the known sample mass and the intensity on the mass 44 detector was used to calculate the weight percent carbonate (i.e., "wt% carbonate") for each sample. Samples (n=181) were analyzed for ^{13}C and $^{18}O_{carb}$ using a Thermo Scientific GasBench II coupled to a Thermo Delta V continuous flow isotope ratio mass spectrometer in the CU Boulder Earth Systems Stable

Isotope Laboratory (CUBES-SIL; RRID SCR-019300). All stable isotope ratios are reported in delta ( ) notation as the per mil (‰) deviation relative to the Vienna Pee Dee Belemnite (VPDB) standard, where = ([(R_{Sample} / $R_{Standard}$) – 1] x 1000), and R is the ratio of the heavier mass isotope to the lighter mass isotope. Repeated measurements of internal and internationalyl accepted carbonate standards (i.e., Icelandic Spar (HIS), NBS19, and CU YULE, an internal Yule marble) yielded precision of ± 0.1 ‰ or better for both ^{13}C and $^{18}O_{carb}$. To correct raw values, the *Isoreader* R package was used to read all raw data files directly into R (Kopf et al., 2021). Values were evaluated for and then corrected for the effects of linearity and drift, if identified. These corrected values, rather than the raw values, were then used in a scale correction. Linearity, drift, and scale corrections to data were done using in-house CUBES-SIL R scripts that utilized *tidyverse* (v. 1.3.1) and *isoprocessor* (v. 0.6.5) R packages. There was a consistent average offset of 0.7‰ and 0.14‰ for bulk $^{13}C_{carb}$ and $^{18}O_{carb}$ values, respectively, for data generated on both the Delta V and 253 Plus. We accounted for this by calculating a sample mean and standard error weighted by the standard error for each analyzed aliquot of sample powder analyzed on the two machines. Errors for ^{13}C and $^{18}O_{carb}$ measurements reported in the text and in all figures represent two standard error (i.e., 2.s.e.) of the mean (Table S2).

3.4 Clumped isotopes (Δ_{47}) analytical procedure

As temperature decreases, it is thermodynamically favorable to form more doubly-substituted carbonate isotopologues that include both the heavy isotopes of carbon and oxygen ($^{13}C^{18}O^{16}O_2{}^{2-}$, termed "clumps") (Eiler, 2007, 2011); this inverse relationship between temperature and "clumping" is used as a paleothermometer (Anderson et al., 2021; Ghosh et al., 2006). Clumped isotope analyses were performed on 58 samples that appeared well preserved based on petrographic inspection, as well as on some samples with identifiable diagenetic fabrics and secondary spar inclusions (Table S3). Calcium carbonate standards (e.g., ETH1–4, IAEA-C1 and C2, Merck, and NBS19) were analyzed at a standard-to-sample ratio of ~1:1 and were used to correct the data to the community accepted Intercarb-Carbon Dioxide Equilibrium Scale (ICDES) (Bernasconi et al., 2021). Only three standards are needed for the correction, and additional standards were used to assess the effectiveness of the data corrections. In addition to carbonate standards, gases equilibrated to 25°C ("equilibrated") and 1000°C ("heated") that spanned a large range of ^{47} values were measured to provide an extended reference frame for samples with very high or low ^{47} values; because all the sample data were within the bounds of the carbonate standards, the gases were not used to correct the samples to the ICDES reference frame.

For samples and carbonate standards, approximately 6–12 mg of carbonate powder was weighed into silver capsules for each analysis. The powders were digested in 90°C phosphoric acid for 45 minutes and the evolved CO_2 was analyzed for the abundance of masses 44-49 of CO_2, and use to determine Δ_{47}, ^{47}, $^{13}C_{carb}$, and $^{18}O_{carb}$ values for each sample. Values are reported as Δ_{47} (‰, ICDES) which is defined as the deviation in the measured ratio of doubly-substituted mass-47 CO_2 ($^{13}C^{18}O^{16}O$) isotopologues to the more abundant mass-44 ($^{12}C^{16}O_2$) isotopologue, $R^{47}_{\mathrm{sample}} = M^{47}_{\mathrm{sample}}/M^{44}_{\mathrm{sample}}$ compared to the expected R^{47} for a stochastic distribution of isotopes (Schauble et al., 2006):

$$_{47}\,(‰) = \left(\frac{R^{47}_{\mathrm{sample}}}{R^{47}_{\mathrm{stochastic}}} - 1\right) * 1000 \tag{1}$$

Δ_{47} data were collected across five sessions between 2019 and 2022 on a Thermo Scientific 253 Plus dual-inlet isotope ratio mass spectrometer in the CUBES–SIL (Table S4). Details about the analytical setup and each run session (AF8 – AF12), including the number of acquisitions, reference gas/sample gas cycles per acquisition, standard gases and carbonates measured, can be found in the supplementary materials. Precision of individual analyses is reported as two standard errors of the mean (2 s.e.) and includes analytical error of each measurement as well as errors associated with the correction lines used (Bernasconi et al., 2021; Dennis et al., 2011; Huntington et al., 2009). All Δ_{47} values for samples reported here, and used to calculate temperatures, are based on averages of 3-9 replicates that were typically analyzed across different sessions (Table S3). Outlier replicates for each sample were culled if they were outside of the two standard deviations of the replicate mean in any isotope. Δ_{47} values were calculated as weighted means of all the replicates, and associated errors were calculated using standard errors of the replicates as the weighting factors, following Huntington et al. (2009). The median of the replicates for each sample was also calculated as a comparison to the weighted mean values for $^{18}O_{water}$ and T($_{47}$) estimates. Mean Δ_{47} precision of carbonate standards across all run sessions is 0.012‰ (± 2.8x10^{-4}, 2s.e.). Temperatures were estimated from the mean $_{47}$ values using the Anderson et al. (2021) calibration line, and temperature uncertainties were estimated by taking into account the Δ_{47} standard error for every sample; all plots show two standard errors (2 s.e.) for T(Δ_{47}). From the measured Δ_{47} temperature and $^{18}O_{carb}$ values, the ^{18}O of the water ($^{18}O_{water}$) in which the carbonate sample precipitated was calculated using the equilibrium fractionation between calcite and water established by Kim and O'Neil (1997). $^{18}O_{water}$ is reported relative to the VSMOW reference frame (Coplen, 2011). Errors for $^{18}O_{water}$ measurements reported in the text and in all figures represent 2 s.e. of the mean and incorporate the error from $_{47}$ measurements.

4 Results

4.1 ^{13}C

Across all NCF facies, ^{13}C values range from approximately −7.05‰ to +2.26‰. For the palustrine facies, the mean ^{13}C value for $Mp_{(wetland)}$ is −4.32‰ (±

0.29‰, 2s.e.) and ranges from –6.23‰ to –3.07‰ (Table 1). The mean ^{13}C value for the Mm$_{(wetland)}$ facies is –4.45‰ (± 0.36‰, 2s.e.) and ranges from –6.23‰ to –3.41‰. The one Gc$_{(channel)}$ sample analyzed has a ^{13}C value of –3.68‰ (± 0.06‰, 2s.e.). The Mb$_{(pond)}$ and associated Mn$_{(soil)}$ facies have the most negative ^{13}C values with average ^{13}C values of –4.79‰ (± 0.56‰, 2s.e.) and –5.42‰ (± 1.37‰, 2s.e.), respectively.

The M$_{(lake)}$ has an average ^{13}C of –3.39‰ (± 0.44‰, 2s.e.) and the Mb$_{(lake)}$ has an average of –1.55‰ (± 1.21‰, 2s.e.). Both the Mb$_{(lake)}$ and M$_{(lake)}$ have considerable variability in ^{13}C values compared to the palustrine facies. The Mb$_{(lake)}$ facies spans from –7.05‰ to +2.15‰ and the M$_{(lake)}$ facies spans from –5.25‰ to +1.29‰. The Fc$_{(lake)}$ facies has an average of –1.03‰ (± 2.07‰, 2s.e.) and ranges from –6.69‰ to +1.05‰.

The NCF secondary spars (*31_spar* and *21.5D_spar*) have ^{13}C values of –2.61‰ (± 0.19‰, 2s.e.) and –6.08‰ (± 0.001‰, 2s.e.), respectively, while the secondary spar from the Ely Limestone has an average ^{13}C value of –0.47‰ (± 0.20‰, 2s.e.). The Ely Limestone has a ^{13}C value of +2.26‰ (± 0.06‰, 2s.e.).

4.2 ^{18}O$_{carb}$

Across all NCF facies, ^{18}O$_{carb}$ values range from approximately –13.80‰ to –1.37‰. The Mm$_{(wetland)}$ facies has the most positive ^{18}O$_{carb}$ values among the four palustrine facies. The Mm$_{(wetland)}$ facies has an average ^{18}O$_{carb}$ value of –8.12‰ (± 0.81‰, 2s.e.) and ranges from –10.96‰ to –4.67‰. The ^{18}O$_{carb}$ values for the Mp$_{(wetland)}$ facies range from approximately –11.35‰ to –5.78‰ with an average ^{18}O$_{carb}$ of –8.96‰ (± 0.46‰, 2s.e.) (Table 1). The Mb$_{(pond)}$ and Mn$_{(soil)}$ facies have average ^{18}O$_{carb}$ values of –9.62‰ (± 0.74‰, 2s.e.) and –8.94 ‰ (± 0.73‰, 2s.e.), respectively. The calcareous conglomerate (Gc$_{(channel)}$) sample analyzed has a ^{18}O$_{carb}$ value of –8.25‰ (± 0.33‰, 2s.e.).

The M$_{(lake)}$ facies, which is the dominant facies preserved in the upper lacustrine section, has an average ^{18}O$_{carb}$ value of –3.58‰ (± 0.80‰, 2s.e.) and has consistently higher ^{18}O$_{carb}$ values than the palustrine facies. The ^{18}O$_{carb}$ values for the Mb$_{(lake)}$ facies, which is the main facies in the lower lacustrine section, range from approximately –13.80‰ to –3.56‰ with an average of –8.07‰ (± 1.33‰, 2s.e.). The spread in ^{18}O$_{carb}$ for the Mb$_{(lake)}$ facies is larger than the variability across the M$_{(lake)}$ facies and all the palustrine facies combined.

The NCF secondary spars (*31_spar* and *21.5D_spar*) have ^{18}O$_{carb}$ values of –9.36‰ (± 0.14‰, 2s.e.) and –14.53‰ (± 0.004‰, 2s.e.), respectively, while the secondary spar from the Ely Limestone has a ^{18}O$_{carb}$ value of –16.99‰ (± 1.04, 2s.e.). The Ely Limestone has a ^{18}O$_{carb}$ value of –6.29‰ (± 0.28‰, 2s.e.).

4.3 ^{18}O$_{water}$

Across all NCF facies, $^{18}O_{water}$ values range from approximately –7.80‰ to +5.00‰. The $Mm_{(wetland)}$ facies has higher $^{18}O_{water}$ values than the $Mp_{(wetland)}$ facies by approximately 2‰ (Table 1). The $Mm_{(wetland)}$ facies has an average $^{18}O_{water}$ value of –0.30‰ (± 0.44‰, 2s.e.) and the $Mp_{(wetland)}$ facies has an average of –2.07‰ (± 0.57‰, 2s.e.). The $Mb_{(pond)}$ and one sample from the $Mn_{(soil)}$ facies have a $^{18}O_{water}$ values of –3.20‰ (± 0.81‰, 2s.e.) and –3.70‰ (± 1.60‰, 2s.e.), respectively. The $Gc_{(channel)}$ sample analyzed has a $^{18}O_{carb}$ value of –2.30‰ (± 2.6‰, 2s.e.).

The $^{18}O_{water}$ values for the $M_{(lake)}$ facies in the upper lacustrine section averages +1.95‰ (± 0.80‰, 2s.e.) and is consistently higher than the palustrine facies. The samples from the lower lacustrine section, dominated by the $Mb_{(lake)}$ facies, are lower than the upper lacustrine samples (–0.44‰ (± 1.42‰, 2s.e.)) and have a broad spread in $^{18}O_{water}$ values (–7.80‰. to +3.70‰).

The NCF secondary spars (*31_spar* and *21.5D_spar*) have $^{18}O_{water}$ values of +8.80‰ (± 2.4‰, 2s.e.) and –4.2‰ (± 1.4‰, 2s.e.), respectively, while the secondary spar from the Ely Limestone has a $^{18}O_{water}$ value of –0.35‰ (± 1.90‰, 2s.e.). The Ely Limestone has a $^{18}O_{water}$ value of +7.90‰ (± 2.20‰, 2s.e.).

4.4 Clumped isotope temperatures (T(Δ47))

There is significant spread (~28 to 68°C) in the T(Δ_{47}) values for the carbonate-bearing facies from the NCF (Table 1). The $Mp_{(wetland)}$ facies has a mean T(Δ_{47}) of 46.8°C (± 3.6°C, 2s.e., n = 15) and the $Mm_{(wetland)}$ facies has a mean T(Δ_{47}) of 52.0°C (± 5.2°C, 2s.e., n = 7). The one $Gc_{(channel)}$ sample analyzed has a T(Δ_{47}) estimate of 43.7°C (± 14.6°C, 2s.e.). Fewer samples of the $Mb_{(pond)}$ (n=3) and $Mn_{(soil)}$ (n=1) facies were fully replicated than the $Mp_{(wetland)}$ and $Mm_{(wetland)}$ facies. $Mb_{(pond)}$ and $Mn_{(soil)}$ have average T($_{47}$) estimates, 49.9°C (± 8.5°C, 2s.e.) and 45.0°C (± 9.0°C, 2s.e.), respectively.

The $M_{(lake)}$ facies has a mean T(Δ_{47}) of 40.3°C (± 2.4°C, 2s.e., n=18), while the $Mb_{(lake)}$ facies has a mean T(Δ_{47}) ~10ºC hotter, at 50.7°C (± 4.4°C, 2s.e., n=11). The one $Fc_{(lake)}$ facies analyzed for T(Δ_{47}) has a temperature estimate of 57.8°C (± 7.0°C, 2s.e., n=1).

The Ely Limestone has an average T($_{47}$) estimate of 96.0°C (± 15.8°C, 2s.e.). The Ely Limestone spar has an average T($_{47}$) estimate of 117.9°C (± 7.2°C, 2s.e.) and the NCF spars (*31_spar* and *21.5D_spar*) have T($_{47}$) estimate of 130.2°C (± 22.2°C, 2s.e.) and 70.4°C (± 9.8°C, 2s.e.), respectively.

Facies	Samples per Facies for ^{13}C and $^{18}O_{carb}$	Median ^{13}C (‰, VPDB)	Mean ^{13}C (‰, VPDB)	^{13}C 2s.e.	^{13}C maximum	^{13}C minimum	Median $^{18}O_{carb}$ (‰, VPDB)	Mean $^{18}O_{carb}$ (‰, VPDB)	$^{18}O_{carb}$ 2s.e.	$^{18}O_{carb}$ maximum	$^{18}O_{carb}$ minimum	Samples per Facies for T(Δ_{47}) and $^{18}O_{water}$	Median $^{18}O_{water}$ (‰, VPDB)	Mean $^{18}O_{water}$ (‰, VPDB)	$^{18}O_{water}$ 2s.e.	$^{18}O_{water}$ maximum	$^{18}O_{water}$ minimum	Median T(Δ_{47}) (°C)	Mean T(Δ_{47}) (°C)	T(Δ_{47}) 2s.e.	T(Δ_{47}) maximum	T(Δ_{47}) minimum
Ely																						
Ely Spar																						
Fc_{lake}																						
$Gc_{channel}$																						
M_{lake}																						
Mb_{lake}																						
Mb_{pond}																						
$Mm_{wetland}$																						
Mn_{soil}																						
$Mp_{wetland}$																						
Spar																						

Table 1. Facies averages including all samples.

5 Discussion

Before it is possible to use the carbon, oxygen, and clumped isotope records from the NCF to interpret the paleoclimate, paleoenvironment, and paleoelevation of the terrestrial western USA in the mid-Cretaceous, we must account for diagenetic changes to the isotopic record. The presence of cross-cutting spar veins, discrete spar crystals of calcite and dolomite, and sparite in the NCF demonstrate that the rocks experienced high temperatures, either from deep burial or interaction with hot fluids from depth, or both. In the following sections, we evaluate possible impacts of diagenesis associated with solid state reordering and/or from hydrothermal fluids, and disentangle these effects from the primary depositional mechanisms that drive isotopic variability (Figure 4).

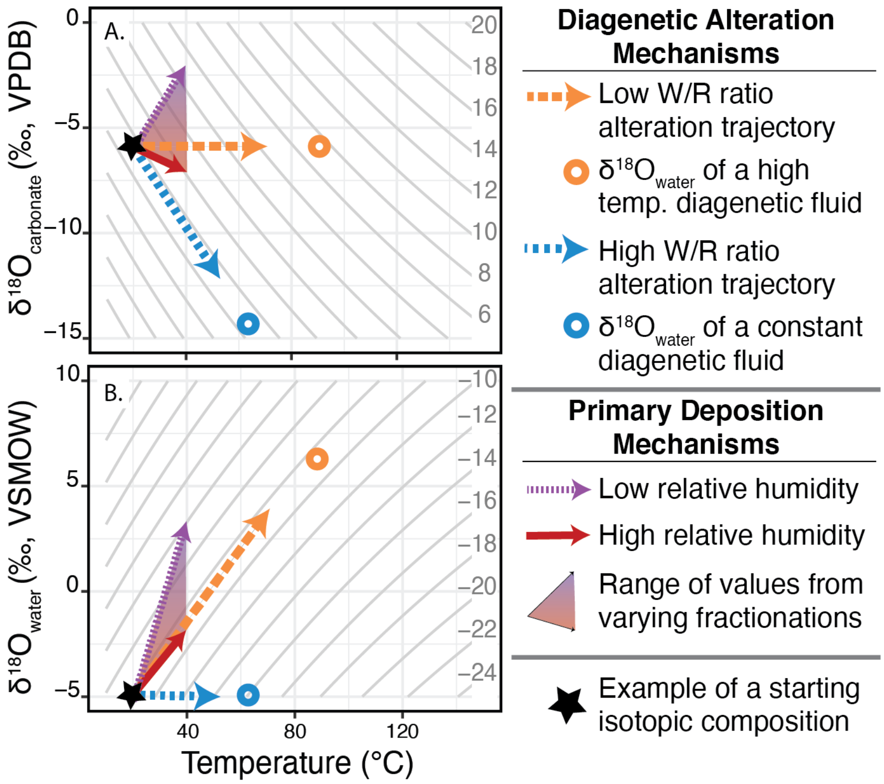

Figure 4. Schematic of $^{18}O_{carb}$ (‰, VPDB) and $^{18}O_{water}$ (‰, VSMOW) plotted against T($_{47}$) estimates (ºC) with trajectories depicting two diagenetic alteration mechanisms and two evaporative enrichment scenarios that could occur on the primary depositional landscape.

5.1 Solid state reordering

Laboratory heating experiments and numerical modeling of bond ordering have shown that Δ_{47} values of calcite samples will reorder if exposed to temperatures in excess of ~100ºC for 10^6–10^8 years (Henkes et al., 2014; Passey & Henkes, 2012). If solid state reordering had significantly impacted T($_{47}$) values from the NCF, we would expect to see little variability in T($_{47}$) and $^{18}O_{water}$ values between carbonate facies at similar stratigraphic heights. In particular, we would expect carbonate facies that are closely interbedded in the palustrine and lacustrine portions of the record, such as $Mp_{(wetland)}$ vs. $Mm_{(wetland)}$ and $M_{(lake)}$ vs. $Mb_{(lake)}$ to preserve similar T($_{47}$) values. Instead, T(Δ_{47}) estimates are distinctive between facies throughout the NCF record (Figure 5 and 6, and Figure S4 and S5).

The burial history the Cretaceous NCF and underlying formations also suggests limited impacts on T($_{47}$) from solid state reordering. The NCF in the southern Diamond Mountains overlies the Permian Carbon Ridge Formation across an unconformity, and is locally projected to overlie the Carboniferous Ely Limestone (Di Fiori et al., 2020; Long et al., 2014; Nolan et al., 1956). This demonstrates that the Paleozoic section in this region was buried at least two times: first during deposition of the Paleozoic sedimentary sequence, and then a second time after exhumation to the surface and burial during deposition of the NCF. Peak temperature estimates for the Ely Limestone in the Grant Range, ~160 km southeast of the NCF type section, of 99ºC and 144ºC were found using Rock-Eval pyrolysis and vitrinite reflectance, respectively (Long & Soignard, 2016). Using the hotter vitrinite reflectance temperature for the Ely Limestone (144ºC) and assuming the average geothermal gradient of ~ 50 ºC/km for this region of the Sevier hinterland during the Cretaceous (e.g., Long & Soignard, 2016; Zuza et al., 2020), the Ely Limestone experienced an approximate burial depth of ~ 3 km. If the peak temperature estimates reflect the first burial of the Carbon Ridge and Ely Limestone, then this implies that the maximum burial of the NCF is not much more than its thickness of ~500 m (Fetrow et al., 2020; Di Fiori et al., 2020; Long et al., 2014). There is very little indication that a thick sequence of younger sedimentary rocks was deposited on top of the NCF. However, this cannot be discounted, and so if the peak temperature estimates instead reflect the second burial of the Carbon Ridge and Ely Limestone, then the combined thickness of these two units of ~1 km, plus the ~500 m thickness of the NCF and assuming the average geothermal gradient of ~ 50 ºC/km for this region of the Sevier hinterland during the Cretaceous (e.g., Long & Soignard, 2016; Zuza et al., 2020), the base of the overlying NCF could not have been buried beyond the estimated 1.5 km and did not experience burial temperatures greater than ~ 75ºC. Based on burial of the NCF to 0.5-1.5 km, it is unlikely that the entirety of NCF type section experienced temperatures >100°C long enough to generate significant solid-state reordering. Given the lack of necessary burial, other mechanisms, such as more localized secondary alteration and/or primary depositional conditions must be responsible for the range of temperatures and isotope values.

5.2 Disentangling hydrothermal diagenesis from primary depositional processes

5.2.1 Framework for evaluating hydrothermal alteration

Plots of $^{18}O_{carb}$ and $^{18}O_{water}$ against T($_{47}$) estimates provide a framework of endmember isotope and temperature scenarios that can be used to identify diagenetic effects on the NCF stable isotope values (Bergmann et al., 2018; Goldberg et al., 2021; Ryb et al., 2021) (Figure 4).

Diagenetic Scenario 1 (Figure 4, blue line): During diagenetic alteration via fluids with a high water to rock (W/R) ratio, as the temperature of the system steadily increases, the $^{18}O_{carb}$ value will evolve along the contour of constant $^{18}O_{water}$ (Figure 4A, diagonal blue line). This assumes that diagenesis occurs in an open system with abundant fluids, which allows the diagenetic fluid to maintain a constant $^{18}O_{water}$ value (Figure 4B, horizontal blue line). Complete isotopic exchange with the diagenetic fluid will create $^{18}O_{carb}$ of the rock that matches the $^{18}O_{carb}$ of secondary carbonate that precipitates directly from the fluid (Figure 4A, blue dot and line).

Diagenetic Scenario 2 (Figure 4, orange line): Under conditions with a very low W/R ratio, $^{18}O_{carb}$ of the rock remains constant (Figure 4A, orange line) as temperature increases (i.e., "rock-buffered" isotopic exchange), while $^{18}O_{water}$ values evolve (Figure 4B, orange line). Solid state reordering, as previously discussed, can be considered an extreme version of this endmember, but in that case, the evolving $^{18}O_{water}$ values are not a true reflection of the $^{18}O_{water}$ of fluids, because no fluids are involved in solid state reordering.

5.2.2 Framework for primary depositional mechanisms

When considering the possible effects of alteration, it is important to also consider how isotopes and temperature will reflect various environmental changes across the primary depositional landscape, as some processes may result in isotopic trends that are similar to alteration trajectories. For example, the wetlands that deposited the $Mp_{(wetland)}$ and $Mm_{(wetland)}$ likely experienced variations in the amount of evaporation or radiative heating of the water and ground, which would have propagated to the $^{18}O_{carb}$, $^{18}O_{water}$, and T($_{47}$) values of these facies. The purple dashed and red solid lines in Figure 4 represent theoretical trajectories in which temperature increases under high and low relative humidity conditions. The degree of fractionation between liquid and vapor ($_{water\text{-}vapor}$) decreases with increasing relative humidity, enabled by increased exchange between the liquid and vapor as the system approaches equilibrium exchange (Chacko et al., 2019; Gonfiantini et al., 2018). Conversely, there is more fractionation between liquid and vapor (higher $_{water\text{-}vapor}$) at lower relative humidity conditions, and therefore, the residual liquid water becomes more enriched in ^{18}O (Dansgaard, 1964; Luz et al., 2009).

Applying this to the NCF, higher $_{water\text{-}vapor}$ resulting from low relative humidity conditions would generate a residual water body, such as a wetland, that is more evaporatively ^{18}O-enriched. Any subsequent carbonate minerals that precipitated from the ^{18}O-enriched water would have higher $^{18}O_{carb}$ values. The shaded region between the theoretical high and low fractionation trajectories represents a gradient of possible isotope compositions that could occur depending on the relative humidity and resulting $_{water\text{-}vapor}$. Evaporative enrichment must be considered given the sedimentological evidence that evaporation was a key driver of depositional heterogeneity in the palustrine environments of the lower NCF type section, such as the presence of mud cracking and pseudo-microkarsting (Fetrow et al., 2020). Notably, the low fractionation scenario (red line) results in evolution of $^{18}O_{carb}$, $^{18}O_{water}$, and T($_{47}$) values that are similar to the trajectories of diagenetic alteration under low W/R conditions, although the upper temperature limit for evaporation in a surface environment is likely lower than for low W/R alteration. Also, these two evaporation scenarios are simplified, and exclude the consideration of other environmental conditions that influence evaporation, such as wind speed, water body surface area, and salinity (Harbeck, 1962). Finally, the lower palustrine and upper lacustrine units in the NCF type section are separated by likely > 5 Myr of deposition and/or sedimentary hiatuses (Figure 2), and therefore, the stratigraphic order may not directly dictate the alteration history of each unit. Accounting for this stratigraphic separation, we will first consider lacustrine data separately from the palustrine data (Figure 5 and Figure 6).

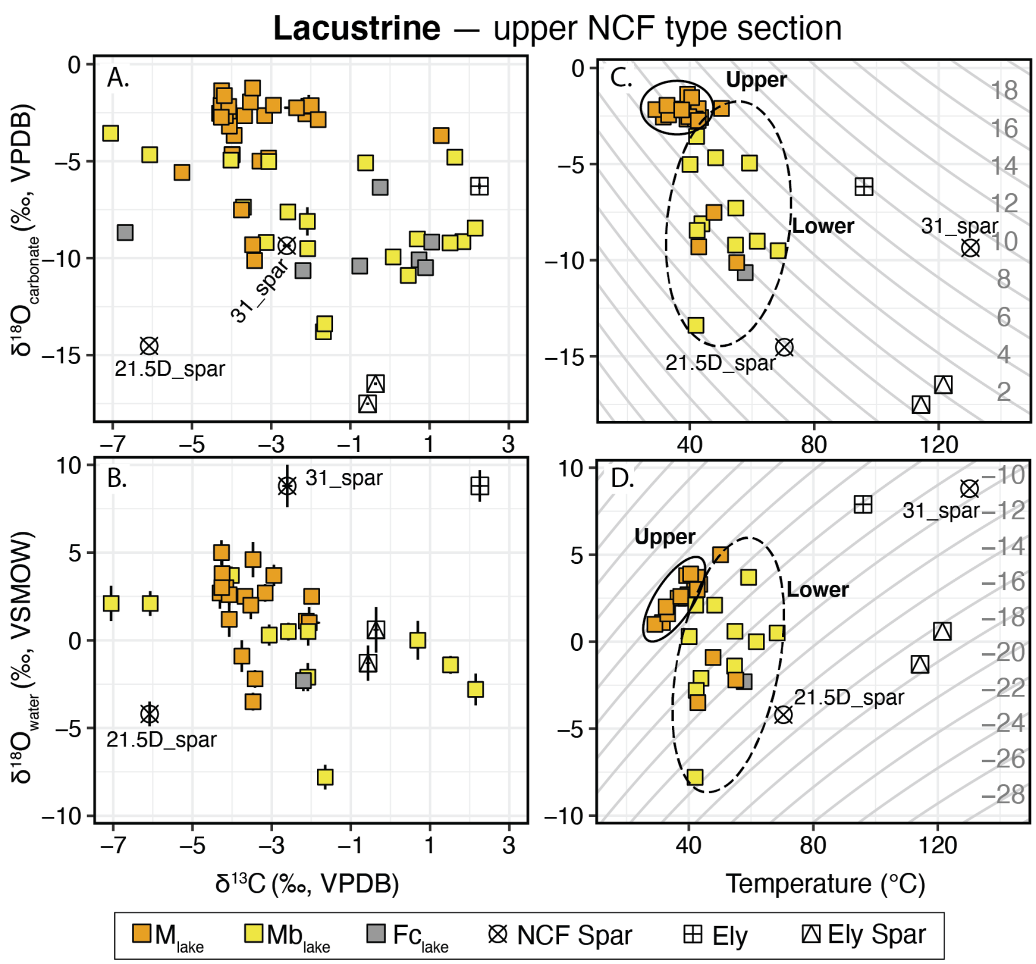

Figure 5. Bivariate plots for lacustrine samples from Stage 3 of the NCF type section. Solid and dashed circles denote lacustrine samples from the upper and lower portion of Stage 3, respectively. Symbols colored by facies. a) ^{13}C (‰, VPDB) vs. ^{18}O$_{carb}$ (‰, VPDB). b) ^{13}C (‰, VPDB) vs. ^{18}O$_{water}$ (‰, VSMOW). Error bars plotted for subplots A and B represent two standard error (2s.e.) about the sample mean and unless visible, error bars are smaller than the datapoint. c) T($_{47}$) estimates vs. ^{18}O$_{carb}$ (‰, VPDB). d) T($_{47}$) estimates

vs. $^{18}O_{water}$ (‰, VSMOW). Error bars were omitted from subplots c. and d. for visual clarity and are reported in Figure 7 and Table S2.

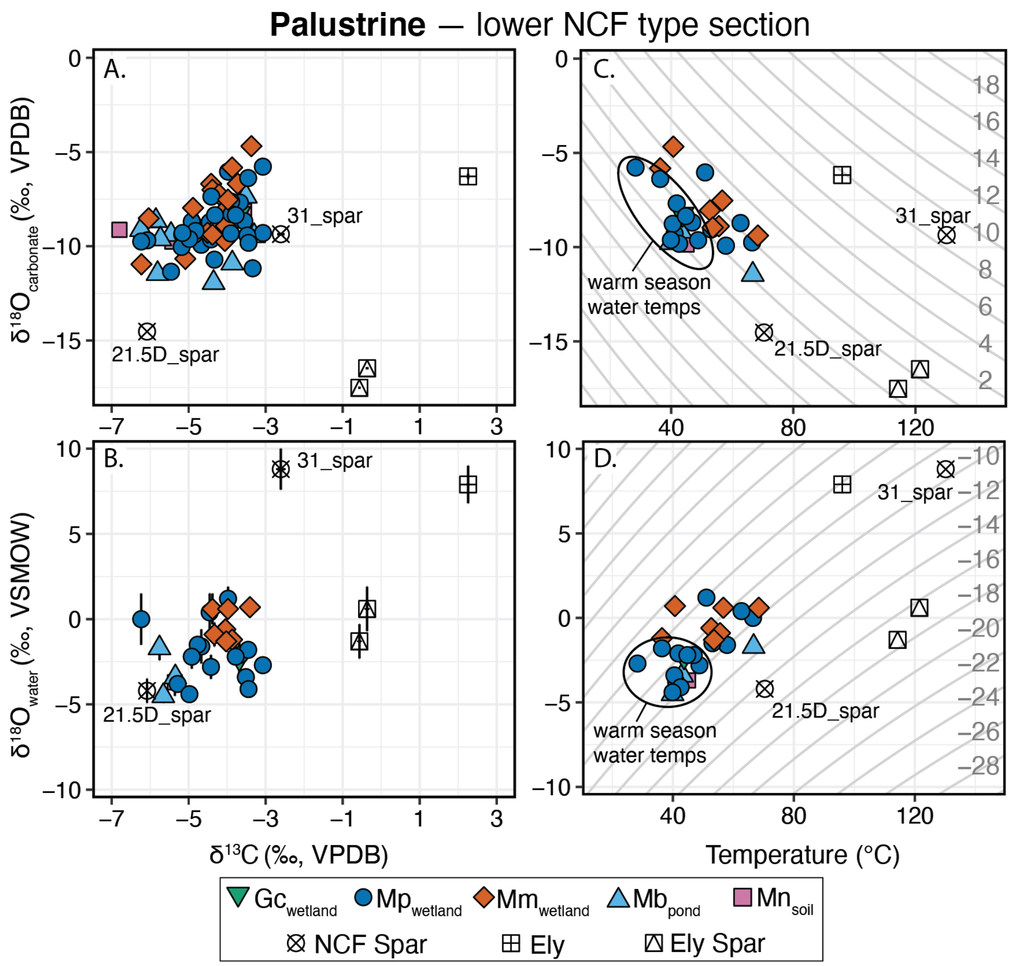

Figure 6. Bivariate plots for palustrine samples from Stage 1 of the NCF type section. Solid circle denotes palustrine samples estimated to preserve T($_{47}$)s representative of primary warm season water temperatures. Symbols shaped and colored by facies. a) ^{13}C (‰, VPDB) vs. $^{18}O_{carb}$ (‰, VPDB). b) ^{13}C (‰, VPDB) vs. $^{18}O_{water}$ (‰, VSMOW). Error bars plotted for subplots A and B represent two standard error (2s.e.) about the sample mean and unless visible, error bars are smaller than the datapoint. Error bars were omitted from subplots C and D for visual clarity and are reported in Figure 7 and Table S2. c) T($_{47}$)estimates vs. $^{18}O_{carb}$ (‰, VPDB). d) T($_{47}$) estimates vs. $^{18}O_{water}$ (‰, VSMOW).

5.2.3 Upper NCF (~112 to 103 Ma) — lacustrine facies

The top of the NCF type section records lacustrine sedimentation in which two interbedded, carbonate-bearing subfacies were deposited, the biomicrite ($Mb_{(lake)}$) and the massive micrite ($M_{(lake)}$). The lower half of the lacustrine samples, which are mostly the $Mb_{(lake)}$ facies, exhibit a wide range in ^{13}C and $^{18}O_{carb}$ values and have isotopic compositions closest to the Ely Limestone and secondary spars from the Ely and NCF samples (Figure 5A,C). This group of lacustrine samples are all from the stratigraphically lower portion of the lake unit (~ 300 to 321 m). The lower lacustrine samples have consistently higher T($_{47}$) estimates and more negative $^{18}O_{water}$ and $^{18}O_{carb}$ values than upper lacustrine samples, regardless of facies type. We observe some spread of the lower lacustrine data along $^{18}O_{water}$ contours (like Scenario 1, blue line) towards the *21.5D_spar* (Figure 5A). The scattering of the lower lacustrine samples toward the Ely Limestone and Ely Spar ^{13}C values and NCF and Ely Spar $^{18}O_{carb}$ values, and the hotter T($_{47}$) estimates suggest that they have been altered by hydrothermal fluids under varying W/R conditions. Some likely were altered by fluids under high W/R conditions (closer to the blue line) while others were under more intermediate W/R settings. In contrast, the $^{18}O_{carb}$ values of the upper lacustrine samples cluster tightly around ~ –2‰, and as a result, they do not track a $^{18}O_{water}$ contour, but rather fall closely along a $^{18}O_{carb}$ contour (Figure 5C).

Additional differences between the upper and lower lacustrine samples become apparent when examining their ^{13}C values. During primary deposition, the ^{13}C of the dissolved inorganic carbon ($^{13}C_{DIC}$) pool of lacustrine and palustrine systems is controlled by exchange of CO_2 between the atmosphere and water, the ^{13}C of inflowing water and the atmosphere, and biological activity in the lake, such as photosynthesis, microbial respiration, and recycling of organic matter (Leng & Marshall, 2004; Talbot, 1990). If the upper and lower lacustrine samples both still preserve primary ^{13}C values, we would expect to see relatively uniform ^{13}C values because both facies would have drawn from the similar DIC pool in the lake, unless one facies experienced a greater influence of isotopic fractionation by biotic processes (e.g., Ingalls et al., 2020; Talbot, 1990). However, the upper lacustrine samples have more negative ^{13}C values with much less spread (mean: –3.39‰ ± 0.44, 2s.e.) than the lower lacustrine samples (mean: –1.55‰ ± 1.21, 2s.e.). During alteration under high W/R conditions, a large volume of fluid can provide more carbon to the system that can isotopically exchange with the carbon of the affected rock. Signals of this isotopic exchange can be detected if the diagenetic fluid has a distinct ^{13}C composition from the rock. This means that a higher W/R for fluids with ^{13}C values that are distinct from the original rock will have a greater impact on ^{13}C of the rock than that same fluid under low W/R exchange. The underlying marine limestones of the Carbon Ridge Formation and Ely Limestone were likely a substantial source for ^{13}C-enriched ^{13}C values in these diagenetic fluids and imprinted their isotopic signature in the lower lacustrine samples altered under relatively high W/R conditions.

Stratigraphically below the lacustrine unit of Stage 3 are a large stack of braided river conglomerates (Figure 2) (Di Fiori et al., 2020; Fetrow et al., 2020). We posit that both the conglomerates and the contact between the conglomerate and lacustrine units may have provided a more porous conduit through which diagenetic fluids could migrate after lithification of the NCF, and it made the lower portion of the lacustrine unit more susceptible to diagenetic alteration. Alternatively, the biomicrite ($Mb_{(lake)}$) facies was more susceptible to diagenetic alteration due to the presence of fossil hash within the dense micrite matrix. Fossil hash could have increased the porosity of the facies, the crystal structure of the biogenic carbonate maybe be more susceptible to alteration, or a combination of the two. However, this facies-based explanation is highly speculative and is not supported by the presence of several $M_{(lake)}$ facies samples that also appear to be reset in the lower section of the lacustrine unit. Rather, the fact that all of the $M_{(lake)}$ facies samples that show similar signs of diagenesis are part of the lower lacustrine section, supports the hypothesis of stratigraphic control on diagenetic fluid migration for this part of the type section. This also explains the bigger temperature range and higher average temperature for the lower lacustrine section.

The isotopic and temperature patterns for upper lacustrine samples require a different explanation. The data from this section shows a tight trend along one $^{18}O_{water}$ contour, and although warm, these samples are some of the coolest NCF T($_{47}$) estimates; T($_{47}$) ranges from 29.1 to 42.8°C, with a mean of 37.7°C (± 2.5°C, 2s.e.) (Table 2). One possible explanation is that they have experienced secondary alteration under low W/R conditions (like Scenario 2, orange line). While we cannot rule this out completely, given that the other data demonstrate the potential for alteration to higher temperatures, it seems unlikely that this suite of samples would not have a similarly high range of temperatures to the $Mb_{(lake)}$ facies.

Alternatively, another explanation for upper lacustrine dataset is that the data reflect temperature control on the $^{18}O_{water}$ at the time of deposition, with minimal influence of evaporation. For middle- to high-latitude regions in our modern climate system, mean annual $^{18}O_{precip}$ values increase by 0.4 to 0.6‰ for every 1ºC increase in mean annual temperature (MAT) based on globally distributed data (Craig, 1965; Dansgaard 1964; Rozanski et al., 1993). $^{18}O_{precip}$ /T slopes may have been smaller relative to the modern spatial relationship when past global climate states were warmer than present and when the relationship is based on temporal datasets of temperature and $^{18}O_{water}$ rather than spatial datasets (Boyle, 1997; Fricke & O'Neil, 1999; Jouzel et al., 1997; Snell et al., 2013). For example, estimates of the temporal $^{18}O_{precip}$ to temperature relationship from the Eocene Bighorn Basin, WY — another mid-latitude, North American, terrestrial sedimentary basin that also formed during greenhouse climate conditions — range from 0.32‰/ºC (± 0.10, 2 s.e.) (Snell et al., 2013) to 0.36–0.39‰/ºC (Secord et al., 2010). The slope of $^{18}O_{water}$/T($_{47}$) for the upper lacustrine samples from the NCF is 0.18‰/ºC (±0.68, 2 s.e.) and is consistent with an expected shallow slope given the hothouse climate of the mid-Cretaceous.

In addition, the NCF lacustrine system is interpreted as a balance-filled lake (as opposed to a closed-basin lake), which is supported by the lack of covariance in ^{13}C and $^{18}O_{carb}$ in the lacustrine facies that would be expect for a closed-basin, evaporation dominated lake (Figure 5A) (Leng & Marshall, 2004; Li & Ku, 1997; Martin-Bello et al., 2019; Talbot, 1990). Together, the similarities of the $^{18}O_{precip}$/T($_{47}$) slopes between the mid-Cretaceous NCF and the Eocene Bighorn Basin, the limited range in T($_{47}$) and the lack of signs of significant evaporation suggest that the upper lacustrine samples preserve primary T($_{47}$)s and reflect temperature-controlled $^{18}O_{precip}$, rather than diagenesis.

5.2.4 Lower NCF (~113 to 112 Ma) — palustrine facies

The lower NCF preserves complexly interbedded palustrine pebbly pelmicrite ($Mp_{(wetland)}$) and mottled micrite ($Mm_{(wetland)}$), pond biomicrite ($Mb_{(pond)}$), and paleosols with carbonate nodules ($Mn_{(soil)}$). The water depth gradient reflected by these facies implies differential effects of radiative heating of water and exposed sediment, pedogenesis, and inundation by nearby river channels on each facies, and provides a framework with which to explain the similarities and differences of these facies (Figure 3).

First, the overlap in ^{13}C values of the palustrine facies indicates that they likely reflect a common DIC pool during carbonate precipitation (Figure 6A/B). The slightly lower ^{13}C values of the mottled micrite compared to the pebbly pelmicrite may result from more frequent subaerial exposure and associated incipient pedogenesis. This would likely increase the amount of soil CO_2 in the DIC pool, driving ^{13}C values lower (e.g., Ehleringer et al., 2000). Second, the palustrine facies show greater variability than the upper lacustrine samples and do not fall particularly along either the $^{18}O_{carb}$ or the $^{18}O_{water}$ contours (Figure 6C/D). This suggests that the palustrine facies did not undergo significant secondary alteration due to hydrothermal fluids, in contrast to the lower lacustrine samples. On the other hand, evidence of mud cracking and pseudo-microkarstification found in the palustrine facies (Fetrow et al., 2020) indicate that evaporation was an active process in the palustrine environment, plausibly generating the spread in the palustrine isotope data (Figure 6).

Third, the mottled micrite samples generally record hotter T($_{47}$) than the pebbly pelmicrite. This pattern agrees well with the palustrine depositional model, where the mottled micrite that formed in shallower wetlands would have warmed more quickly with diurnal and seasonal temperature variations compared to wetland areas with deeper water. The T($_{47}$) values as high as 68°C in the mottled micrite facies (average of 53ºC) (Table 1) may seem too high to be “reasonable” Earth surface temperatures, but this overlooks the extreme temperatures that are possible in certain depositional settings. The shallower palustrine environments represented by the mottled micrite facies were likely dark mudflats with sparse to no vegetation to provide shade (Fetrow et al., 2020). Studies of modern bare-skin surface temperatures — defined as the surface temperature that bare, un-vegetated ground can reach due to a combination of ambient air temperature and direct radiative heating — show that bare-skin temperatures can reach temperatures up to 70ºC (158ºF), 30–50ºC hotter than air temperature, depending on the color of the exposed regolith and vegetative extent (Mildrexler et al., 2011) and surface sediment temperatures can vary up to ~28°C in one diurnal cycle on tidal flats (Cho et al., 2005). T($_{47}$) records the temperature of mineral precipitation, and so have the potential to preserve hot bare-skin temperatures rather than average water or ground temperatures. The mottled micrite T($_{47}$) values are all within the range of these modern surface temperature extremes, and so it is plausible that these hot temperatures do reflect primary conditions. Additionally, since carbonates are reversely soluble minerals, it is possible that more carbonate is produced during relatively short but very warm events, resulting in extreme temperatures being over-represented in a carbonate sample, relative to what a true temporal average of temperature was during sedimentation.

Even if the samples from the mottled micrite facies are unaltered, if their T(Δ_{47}) values reflect bare-skin temperatures, the mottled micrite facies data should not used to interpret "ambient" regional climate or climatic trends through time. These data still provide some constraint on overall response of the environment to the climate of the time, however. For example, an environment that can experience extreme surface temperatures of 50°C to 70°C will impose, for even short amounts of time, restrictions on the flora and fauna that can survive in these settings. This may be one reason that the NCF palustrine carbonates show few signs of vegetative colonization; it would have been difficult for plants to persist if the shallow portions on the wetlands frequently dried up and experienced extreme warmth.

This discussion highlights the difficulty of setting an upper T(Δ_{47}) boundary below which all samples reflect ambient climate at the time of deposition. That said, the pebbly pelmicrite facies was deposited in deeper portions of the palustrine environment and does not preserve sedimentary features of extreme desiccation or subaerial exposure, unlike the mottled micrite. We expect, therefore, the pebbly pelmicrite facies to record temperatures closest to average warm-season conditions. With one exception, there are no palustrine samples with T(Δ_{47}) estimates cooler than 35°C, and the pebbly pelmicrite samples have a weighted mean of 41.3°C (± 3.6°C, 2s.e.) (Table 2). Therefore, we interpret that the lower temperature zone of 35–40°C as a reasonable estimate of the warm season water temperatures present on the landscape during the time of deposition of these palustrine carbonates.

Setting	Facies	Median ^{13}C (‰, VDPB)	Mean ^{13}C (‰, VDPB)	^{13}C 2s.e.	^{13}C maximum
Palustrine	$Mp_{wetland}$	-3.72	-4.05	0.49	-3.07
Palustrine	Mn_{soil}	-5.36	-5.36	0.10	-5.36
Palustrine	Mb_{pond}	-5.50	-5.50	0.31	-5.35
Palustrine	$Gc_{channel}$	-3.68	-3.68	0.06	-3.68
Lacustrine	M_{lake}	-3.62	-3.44	0.46	-1.99

Table 2. Facies averages calculated only with samples deemed to preserve signals of primary deposition. Samples with evidence of secondary alteration have been excluded.

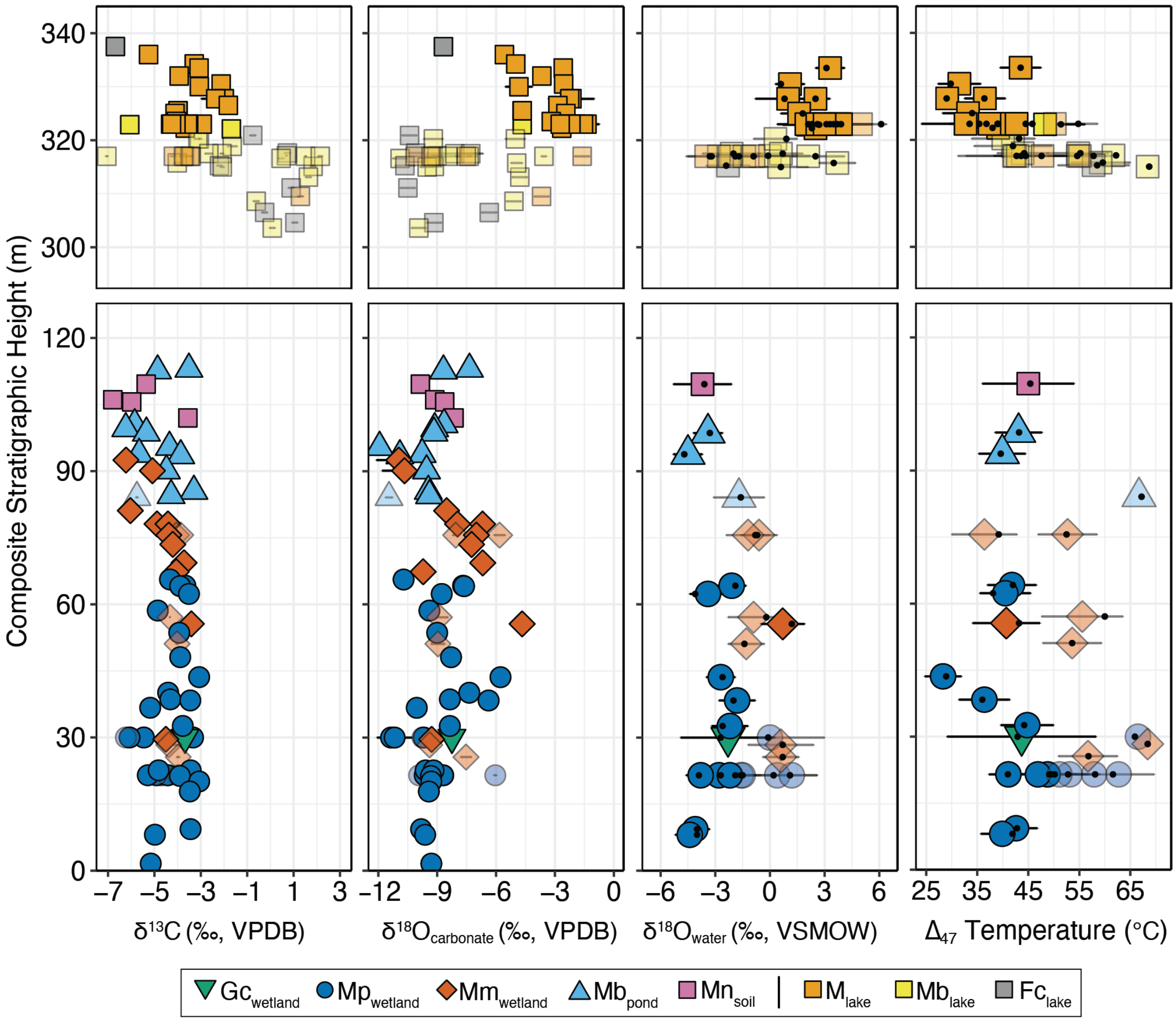

Figure 7. Weighted mean values for ^{13}C, $^{18}O_{carb}$, $^{18}O_{water}$, and $T(\Delta_{47})$ versus composite stratigraphic height for the NCF type section. Note the stratigraphic break between the lower and upper NCF units. Means are weighted by standard error for each sample replicate. Error bars represent two standard errors (2s.e.) about the sample mean. Unless visible, error bars are smaller than the datapoint. For comparison, black dots in $^{18}O_{water}$ and Δ_{47} temperature estimate panels represent the median value of the replicates analyzed for

each sample. Partially transparent symbols were either affected by secondary alteration (i.e., $Mb_{(lake)}$ and $Fc_{(lake)}$ facies) or do not represent ambient environmental conditions (e.g., $Mm_{(wetland)}$ facies). Opaque symbols indicate samples used to assess mid-Cretaceous paleoclimate conditions.

6 Paleoclimate Implications

6.1 Comparison of NCF temperatures to other records

The palustrine carbonate unit of the lower NCF type section (pebbly pelmicrite facies ($Mp_{(wetland)}$); ~113–112 Ma) and the upper portion of the balance-filled lacustrine unit (micrite facies ($M_{(lake)}$); ~112–103 Ma) preserve average warm season water temperatures of 41.1°C (± 3.6°C, 2s.e.) and 37.8°C (± 2.5°C, 2s.e.), respectively (Figure 7 and Table 2). These high temperatures from the mid-Cretaceous Sevier hinterland imply warm overall regional climate conditions and agree closely with a hot global climatic setting of the mid-Cretaceous just before the Cretaceous Thermal Maximum. While the temperatures recorded in the NCF at first glance seem extreme, they are similar or only slightly warmer than mid-Cretaceous sea surface and terrestrial temperature estimates, and for terrestrial records from other hothouse climate periods. For example, tropical sea surface temperature estimates derived from TEX_{86} in Albian–Santonian (113–83 Ma) sediments in the western equatorial Atlantic indicate temperatures ranging from ~31–35ºC (Forster et al., 2007). Oxygen isotopes and Mg/Ca ratios in Albian to Santonian (~113–83 Ma) planktonic foraminifera support upper ocean temperature estimates between 33 to 42ºC for the tropical Atlantic (Bice et al., 2006). On land, mid-Cretaceous $T(\Delta_{47})$ estimates from Cedar Mountain Formation (Utah, USA) paleosol and palustrine carbonates range from 30 to 39ºC which overlaps with NCF $T(\Delta_{47})$ estimates (Ludvigson et al., 2010, 2015; Suarez et al., 2021). Like our samples, these temperatures likely represent carbonate formation during the warm season as well as the potential influence of radiative heating. While there are few terrestrial records from this time with which to compare our data, it is notable that these temperatures are similar to other records from times with hothouse climates. $T(\Delta_{47})$ values from paleosol carbonates from the Bighorn Basin (Wyoming, USA) have peak temperatures of ~40–42°C at the Paleocene-Eocene Thermal Maximum (PETM) and just before the Early Eocene Climatic Optimum (EECO) (Snell et al., 2013). In general, foraminiferal ^{18}O compilations suggest similar temperature estimates for the mid-Cretaceous and Early Eocene (which represents the apex of Cenozoic warmth) and so the similarity in peak temperatures for these records is supported by the similarities in the marine records (Huber et al., 2018).

6.2 Implications for hydroclimate

While $^{18}O_{water}$ values estimated from $T(\Delta_{47})$ records can provide insights into the regional hydroclimate during the mid-Cretaceous, factors like moisture source, source water ^{18}O and transport distance, and the extent of evaporative modification of $^{18}O_{water}$ values will all impact $^{18}O_{water}$ values of soils, wetlands, and lakes. There is significant uncertainty in paleo-wind directions and thus moisture sources for the western USA in the mid-Cretaceous. Climate modeling for North America at ~90 Ma (Turonian), which corresponds most closely with deposition of the upper NCF lacustrine unit, suggests that during the winter the western USA received westerly winds from the Pacific Ocean, while during the summer moisture came from the east, derived from the WIS (Elder, 1988; Poulsen et al., 1999). In contrast, this same study suggests significantly different paleowind directions, and thus moisture sources, for the western USA at ~100 Ma (Albian/Cenomanian) where winds came from the west in the winter and from either the Pacific or the Arctic Oceans during the summer. These two times were substantially different in the western USA with respect to the degree of incursion of the Western Interior Seaway; 100 Ma featuring moderate encroachment of marine waters from the north into interior North America, and therefore greater transport distances to our site, while at 90 Ma the seaway was fully connected from north to south, which implies shorter transport distances if/when moisture sources came from the east of the site (Cobban & Gill, 1973; McDonough & Cross, 1991; Scott et al., 2018). For the NCF location, moisture coming from the Gulf and/or Arctic during the Aptian/Albian travelled farther than moisture coming from the Pacific, while moisture coming from the Pacific may have encountered some topographic relief on its way to the NCF basin. Given that the degree of Rayleigh fractionation associated with transport of moisture is the net effect of temperature, transport distance, and elevation (among other effects, e.g., Rozanski et al., 1993), it is difficult to determine which moisture source would have been more ^{18}O-depleted by the time it reached the basin. In addition, the high temperatures, summer bias, and high humidity of the time would have minimized the extent of fractionation due to transport (e.g., Poulsen & Jeffery, 2011; Rozanski et al., 1993). These combined effects could have created in meteoric water that was minimally ^{18}O-depleted at the NCF site relative to its marine source water, regardless of the specific moisture source.

This has implications for evaluating the impact of evaporation on the $^{18}O_{water}$ values estimated in this study. While the high $^{18}O_{water}$ values could suggest evaporative modification, if the meteoric waters were minimally fractionated during transport, then minimal evaporation is needed to explain the relatively high wetland and lake $^{18}O_{water}$ values. This is consistent with the shallow slope of our lake water $^{18}O_{water}$/ $T(\Delta_{47})$ relationship, and the other indications that this region was humid at the time (e.g., Hasegawa et al., 2012; Qiao et al., 2022). If the high $^{18}O_{water}$ values do not reflect significant evaporation in general, then this process is unlikely to explain the +5‰ shift between the average palustrine $^{18}O_{water}$ for Stage 1 (−2.97‰ ±1.12‰, 2s.e.) and the Stage 3 lacustrine average (+2.71‰ ± 0.66‰, 2s.e.) (Figure 7). This shift may result instead from a change in dominant moisture source(s) to the NCF basin during its ~15 Myr depositional record. As discussed above, at the time of NCF Stage 3 deposition, the Western Interior Seaway had inundated the central North American continent and global climate was warmer than during Stage 1. Together, this could have caused both a seasonal shift in moisture sources to the NCF basin during this time (Suarez et al., 2011; Ufnar et al., 2002; White et al., 2001), and further reduced transport-related fractionation, resulting in higher ^{18}O of meteoric water in the region.

7 Conclusions

We presented ^{13}C, $^{18}O_{carb}$, $^{18}O_{water}$, and T($_{47}$) estimates for the Newark Canyon Formation from central Nevada to examine terrestrial paleoclimate conditions of the Western USA during the mid-Cretaceous. Pairing our large stable isotope and T($_{47}$) dataset with a detailed depositional facies model provides an example of how paleoclimate and paleoenvironmental signals can be extracted from ancient and heterogeneous terrestrial carbonate archives. We use $^{18}O_{carb}$–$^{18}O_{water}$–T($_{47}$) contour plots as endmember scenarios to deconvolve the influence of complex primary deposition from the effects of diagenetic processes. The estimated burial depth and peak temperatures of the NCF rule out significant solid-state reordering. While the upper and lower portions of the lacustrine unit experienced differential fluid-mediated diagenesis, because of the stratigraphic proximity of the lower lacustrine section to more porous underlying conglomerate units. In contrast, the upper lacustrine unit may preserve primary temperatures and $^{18}O_{water}$ values of catchment-integrated precipitation. The strong covariance of $^{18}O_{water}$ with T($_{47}$) for the upper lacustrine unit suggest that temperature is the dominant control on $^{18}O_{precip}$ for this period of deposition.

We find that isotopic records from the palustrine facies preserved in the lower NCF type section reflect the heterogeneity of the complex environment in which they formed. The pebbly pelmicrite facies records temperatures closer to average ambient conditions that reflect warm season water temperatures of 35–40°C. In contrast, due to formation in shallow water, some of the mottled micrite facies record more extreme temperatures on the landscape (i.e., bare-skin temperatures). This facies demonstrates that even primary carbonates can record extremely high temperatures that are unaltered but not representative of ambient climate. For this reason, facies that capture extreme temperature conditions could be used to inform paleobotanical and paleoecological questions such as habitability or temperature resiliency of specific species. Additionally, extreme conditions T($_{47}$) estimates could be used to validate paleoclimate models that seek to estimate land surface temperatures, not just air temperatures. These findings are consistent with the general interpretation of the mid-Cretaceous as an extremely hot and humid time.

7 Acknowledgements

Field work and sample collection in Nevada was conducted on the unceded current and ancestral homelands of the Newe (Western Shoshone people). Laboratory work conducted at the University of Colorado Boulder was done on the unceded ancestral lands of the Ute, Cheyenne, and Arapaho peoples. This work was supported by a U.S National Science Foundation (NSF) grant awarded to KES (EAR-1524785), SPL (EAR-1524765), and JB (EAR-1524853), and an NSF Graduate Research Fellowship under Grant No. DGE-1650115 and a University of Colorado Boulder Geological Sciences Department Marcy and Bruce Benson Graduate Research Fellowship awarded to ACF. Any opinions, findings, and conclusions or recommendations expressed in this material are those of the author(s) and do not necessarily reflect the views of the National Science Foundation. We are grateful to Anna Todd and Kacey Connolly for their assistance and hard work in the field, and to Brett Davidheiser-Kroll for his support in the laboratory throughout this project. CUBES–SIL is a CU Boulder Core Facility associated with RRID: SCR_019300.

8 Open Research

All raw and processed stable isotope data files, RStudio data processing scripts using software language R (R Core Team, 2020; RStudio Team, 2020), and corrected data spreadsheets are available in an Open Science Framework repository (https://osf.io/uwqzk/?view_only=8a1d34e4e6ad4d14822a8aaf3c49ffc8). Stable isotope geochemistry data from different analytical sessions were compiled and averaged using an R script which is also available in the OSF repository and includes explanations for which sample replicate analyses were culled. This compilation R script includes all figure making code as well.

9 References

Alonso-Zarza, A. M. (2003). Palaeoenvironmental significance of palustrine carbonates and calcretes in the geological record. *Earth-Science Reviews*, 60(3–4), 261–298. https://doi.org/10.1016/S0012-8252(02)00106-X

Alonso-Zarza, A. M., & Dorado-Valiño, M. (2006). A recent analogue for palustrine carbonate environments: the Quaternary deposits of Las Tablas de Daimiel wetlands, Ciudad Real, Spain. In A. M. Alonso-Zarza & L. H. Tanner (Eds.), *Paleoenvironmental Record and Applications of Calcretes and Palustrine Carbonates* (pp. 153–168). https://doi.org/10.1130/2006.2416(10)

Alonso-Zarza, A. M., Meléndez, A., Martín-García, R., Herrero, M. J., & Martín-Pérez, A. (2012). Discriminating between tectonism and climate signatures in palustrine deposits: Lessons from the Miocene of the Teruel Graben, NE Spain. *Earth-Science Reviews*, 113(3–4), 141–160. http://dx.doi.org/10.1016/j.earscirev.2012.03.011

Alonso-Zarza, A. M., Genise, J. F., & Verde, M. (2011). Sedimentology, diagenesis and ichnology of Cretaceous and Palaeogene calcretes and palustrine carbonates from Uruguay. *Sedimentary Geology*, 236(1–2), 45–61. https://doi.org/10.1016/j.sedgeo.2010.12.003

Alonso-Zarza, A. M., & Wright, V. P. (2010a). Chapter 5 Calcretes. Developments in *Sedimentology*, 61(C), 225–267. https://doi.org/10.1016/S0070-4571(09)06105-6

Alonso-Zarza, A. M., & Wright, V. P. (2010b). Palustrine carbonates - Carbonates in Continental Settings: Facies, Environments, and Processes. In A.

M. Alonso-Zarza & L. H. Tanner (Eds.), Carbonates in Continental Settings: Facies, Environments, and Processes (pp. 103–131). Elsevier.

Anderson, N. T., Kelson, J. R., Kele, S., Da, M., Bonifacie, M., Horita, J., Mackey, T.J., John, C.M., Kluge, T., Petschnig, P., Jost, A.B., Huntington, K.W., Bernasconi, S.M., and Bergmann, K.D. (2021). A unified clumped isotope thermometer calibration (0.5 − 1100 °C) using carbonate-based standardization, Geophysical Research letters, 48, 1–22. https://doi.org/10.1029/2020gl092069

Andrzejewski, K., & Tabor, N. J. (2020). Paleoenvironmental and paleoclimatic reconstruction of Cretaceous (Aptian-Cenomanian) terrestrial formations of Texas and Oklahoma using phyllosilicates. *Palaeogeography, Palaeoclimatology, Palaeoecology*, 543(November 2019), 109491. https://doi.org/10.1016/j.palaeo.2019.109491

Arenas-Abad, C., Vázquez-Urbez, M., Pardo-Tirapu, G., & Sancho-Marcén, C. (2010). Chapter 3: Fluvial and Associated Carbonate Deposits. In *Carbonates in Continental Settings* (Vol. 61, pp. 133–175). Elsevier. https://doi.org/10.1016/S0070-4571(09)06103-2

Barron, E. J. (1983). A warm, equable Cretaceous: The nature of the problem. *Earth Science Reviews*, 19(4), 305–338. https://doi.org/10.1016/0012-8252(83)90001-6

Barron, E. J., Hay, W. W., & Thompson, S. (1989). The hydrologic cycle: A major variable during Earth history during earth history. *Palaeogeography, Palaeoclimatology, Palaeoecology*, 75, 157–174. https://doi.org/10.1016/0031-0182(89)90175-2

Barron, E. J., Fawcett, P. J., Pollard, D., & Thompson, S. (1993). Model simulations of the Cretaceous climates: role of geography and carbon dioxide. *Philosophical Transactions of the Royal Society of London*, 341, 307–316.

Barron, E. J., & Washington, W. M. (1982). Cretaceous Climate: a comparison of atmospheric simulations with the geologic record. *Palaeogeography, Palaeoclimatology, Palaeoecology*, 40, 103–133. https://doi.org/10.1016/0031-0182(82)90086-4

Barron, E. J., & Washington, W. M. (1984). The role of geographic variables in explaining paleoclimates: results from Cretaceous climate model sensitivity studies. *Journal of Geophysical Research*, 89(D1), 1267–1279. https://doi.org/10.1029/JD089iD01p01267

Bergmann, K. D., Finnegan, S., Creel, R., Eiler, J. M., Hughes, N. C., Popov, L. E., & Fischer, W. W. (2018). A paired apatite and calcite clumped isotope thermometry approach to estimating Cambro-Ordovician seawater temperatures and isotopic composition. *Geochimica et Cosmochimica Acta*, 224, 18–41. https://doi.org/10.1016/j.gca.2017.11.015

Bernasconi, S. M., Daëron, M., Bergmann, K. D., Bonifacie, M., Meckler, A. N., Affek, H. P., Anderson, N., Bajnai, D., Barkan, E., Beverly, E., Blamart, D., Burgener, L., Calmels, D., Chaduteau, C., Clog, M., Davidheiser-Kroll, B., Davies, A., Dux, F., Eiler, J., Elliott, B., Fetrow, A. C., Fiebig, J., Goldberg, S., Hermoso, M., Huntington, K.W., Hyland, E., Ingalls, M., Jaggi, M., John, C. M., Jost, A. B., Katz, S., Kelson, J., Kluge, T., Kocken, I.J., Laskar, A., Leutert, T.J., Liang, D., Lucarelli, J., Mackey, T. J., Mangenot, X., Meinicke, N., Modestou, S.E., Müller, I.A., Murray, S., Neary, A., Packard, N., Passey, B. H., Pelletier, E., Petersen, S., Piasecki, A., Schauer, A., Snell, K. E., Swart, P. K., Tripati, A., Upadhyay, D., Vennemann, T., Winkelstern, I., Yarian, D., Yoshida, N., Zhang, N., and Ziegler, M. (2021). InterCarb: A community effort to improve inter-laboratory standardization of the carbonate clumped isotope thermometer using carbonate standards. *Geochemistry, Geophysics, Geosystems*, 22, 1–25. https://doi.org/10.1029/2020gc009588

Bice, K. L., Birgel, D., Meyers, P. A., Dahl, K. A., Hinrichs, K. U., & Norris, R. D. (2006). A multiple proxy and model study of Cretaceous upper ocean temperatures and atmospheric CO2 concentrations. *Paleoceanography*, 21(2), 1–17. https://doi.org/10.1029/2005PA001203

Blakey, D. (2020). DeepTimeMaps. deeptimemaps.com

Bonde, J. W., Hilton, R. P., Jackson, F. D., & Druschke, P. A. (2015). Fauna of the Newark Canyon Formation (Lower Cretaceous), East-Central Nevada. *Geological Society of Nevada 2015 Symposium*, (April), 139–150. https://www.researchgate.net/publication/275519952%0AFauna

Boyle, E. A. (1997). Cool tropical temperatures shift the global ^{18}O-T relationship: An explanation for the ice core ^{18}O-borehole temperature conflict? *Geophysical Research Letters*, *24*(3), 273–276.

Breecker, D. O., Sharp, Z. D., & McFadden, L. D. (2009). Seasonal bias in the formation and stable isotopic composition of pedogenic carbonate in modern soils from central New Mexico, USA. *Geological Society of America Bulletin*, 121(3/4), 630–640. http://gsabulletin.gsapubs.org/content/121/3-4/630.short

Brouwers, E. M., Clemens, W. A., Spicer, R. A., Ager, T. A., Carter, L. D., & Sliter, W. V. (1987). Dinosaurs on the North Slope, Alaska: High latitude, latest cretaceous environments. *Science*, 237(4822), 1608–1610. https://doi.org/10.1126/science.237.4822.1608

Van Buer, N. J., Miller, E. L., & Dumitru, T. A. (2009). Early Tertiary paleogeologic map of the northern Sierra Nevada batholith and the northwestern Basin and Range. *Geology*, 37(4), 371–374. https://doi.org/10.1130/G25448A.1

Burchfiel, B. C., Lipman, P. W., & Zoback, M. L. (1992). Introduction. In B. C. Burchfiel, P. W. Lipman, & M. L. Zoback (Eds.), *The Cordilleran Orogen: Conterminous US* (pp. 1–6). Geological Society of America.

Burgener, L., Huntington, K. W., Hoke, G. D., Schauer, A., Ringham, M. C., Latorre, C., & Díaz, F. P. (2016). Variations in soil carbonate formation and seasonal bias over >4 km of relief in the western Andes (30°S) revealed by clumped isotope thermometry. *Earth and Planetary Science Letters*, *441*(C), 188–199. Retrieved from http://dx.doi.org/10.1016/j.epsl.2016.02.033

Burgener, L. K., Huntington, K. W., Sletten, R., Watkins, J. M., Quade, J., & Hallet, B. (2018). Clumped isotope constraints on equilibrium carbonate formation and kinetic isotope effects in freezing soils. *Geochimica et Cosmochimica Acta*, *235*, 402–430. https://doi.org/10.1016/j.gca.2018.06.006

Carroll, A. R., & Bohacs, K. M. (1999). Stratigraphic classification of ancient lakes: Balancing tectonic and climatic controls. *Geology*, 27(2), 99–102. https://doi.org/10.1130/0091-7613(1999)027<0099:SCOALB>2.3.CO;2

Case, J. A., Martin, J. E., Chaney, D. S., Reguero, M., Marenssi, S. A., Santillana, S. M., & Woodburne, M. O. (2000). The first duck-billed dinosaur (family hadrosauridae) from Antarctica. *Journal of Vertebrate Paleontology*, 20(3), 612–614. https://doi.org/10.1671/0272-4634(2000)020[0612:TFDBDF]2.0.CO;2

Chacko, T., Cole, D. R., & Horita, J. (2019). Equilibrium oxygen, hydrogen, and carbon isotope fractionation factors applicable to geologic systems. *Stable Isotope Geochemistry*, 43(1977), 1–81.

Cho, Y. K., Kim, T. W., You, K. W., Park, L. H., Moon, H. T., Lee, S. H., & Youn, Y. H. (2005). Temporal and spatial variabilities in the sediment temperature on the Baeksu tidal flat, Korea. *Estuarine, Coastal and Shelf Science*, *65*(1–2), 302–308. https://doi.org/10.1016/j.ecss.2005.06.010

Cobban, W. A., & Gill, J. R. (1973). Stratigraphy and Geologic History of the Montana Group and Equivalent Rocks. Montana, Wyoming and North and South Dakota. Dakota. G*eological Survey Professional Paper*, (776), 1–37.

Coplen, T. B. (2011). Guidelines and recommended terms for expression of stable-isotope-ratio and gas-ratio measurement results. *Rapid Communications in Mass Spectrometry*, 25(17), 2538–2560. https://doi.org/10.1002/rcm.5129

Cowardin, L. M., Carter, V., Golet, F. C., & LaRoe, E. T. (1979). Classification of Wetlands and Deepwater Habitats of the United States. *US Department of Interior, Fish and Wildlife Service*. https://doi.org/FWS/OBS-79/31

Craig, H. (1965). The measurement of oxygen isotope paleotemperatures. In E. Tongiorgi (Ed.), *Stable Isotopes in Oceanographic Studies and Paleotemperatures* (pp. 161–182).

Dansgaard, W. (1964). Stable isotopes in precipitation. *Tellus*, 16(4), 436–468. http://tellusa.net/index.php/tellusa/article/view/8993

David, L. (1941). Leptolepis nevadensis, a New Cretaceous Fish. *Journal of Paleontology*, 15(3), 318–321. https://www.jstor.org/stable/1298900

DeCelles, P. G. (2004). Late Jurassic to Eocene evolution of the Cordilleran thrust belt and foreland basin system, western U.S.A. *American Journal of*

Science, 304(2), 105–168. https://doi.org/10.2475/ajs.304.2.105

DeCelles, P. G., & Coogan, J. C. (2006). Regional structure and kinematic history of the Sevier fold-and-thrust belt, central Utah. *Geological Society of America Bulletin*, 118(2006), 841–864. https://doi.org/10.1130/B25759.1

DeCelles, P. G., & Graham, S. A. (2015). Cyclical processes in the North American Cordilleran orogenic system. *Geology*, 43(6), 499–502. https://doi.org/10.1130/G36482.1

Dee, S. G., Morrill, C., Kim, S. H., & Russell, J. M. (2021). Hot Air, Hot Lakes, or Both? Exploring Mid-Holocene African Temperatures Using Proxy System Modeling. *Journal of Geophysical Research: Atmospheres*, 126(10), 1–23. https://doi.org/10.1029/2020JD033269

Dennis, K. J., Affek, H. P., Passey, B. H., Schrag, D. P., & Eiler, J. M. (2011). Defining an absolute reference frame for “clumped” isotope studies of CO2. *Geochimica et Cosmochimica Acta*, 75(22), 7117–7131. http://dx.doi.org/10.1016/j.gca.2011.09.025

Dewey, J. F., & Bird, J. M. (1970). Mountain Belts and New Global Tectonics. *Journal of Geophysical Research*, 75(14), 2625–2647. https://doi.org/10.1029/JB075i014p02625

Dickinson, W. R. (2004). Evolution of the North American Cordillera. *Annual Review of Earth and Planetary Sciences*, 32, 13–45. https://doi.org/10.1146/annurev.earth.32.101802.120257

Druschke, P., Hanson, A. D., Wells, M. L., Gehrels, G. E., & Stockli, D. (2011). Paleogeographic isolation of the Cretaceous to Eocene Sevier hinterland, east-central Nevada: Insights from U-Pb and (U-Th)/He detrital zircon ages of hinterland strata. *Geological Society of America Bulletin*, 123(5–6), 1141–1160. https://doi.org/10.1130/B30029.1

Dunagan, S. P., & Driese, S. G. (1999). Control of Terrestrial Stabilization on Late Devonian Palustrine Carbonate Deposition: Catskill Magnafacies, New York, U.S.A. *Journal of Sedimentary Research*, Vol. 69 (1, 1–12. http://search.datapages.com/data/doi/10.1306/D4268A8B-2B26-11D7-8648000102C1865D

Ehleringer, J. R., Buchmann, N., & Flanagan, L. B. (2000). Carbon isotope ratios in belowground carbon cycle processes. *Ecological Applications*, 10(2), 412–422. https://doi.org/10.1890/1051-0761(2000)010[0412:CIRIBC]2.0.CO;2

Eiler, J. M. (2007). “Clumped-isotope” geochemistry-The study of naturally occurring, multiply-substituted isotopologues. *Earth and Planetary Science Letters*, 262(3–4), 309–327. https://doi.org/10.1016/j.epsl.2007.08.020

Eiler, J. M. (2011). Paleoclimate reconstruction using carbonate clumped isotope thermometry. *Quaternary Science Reviews*, 30(25–26), 3575–3588. https://doi.org/10.1016/j.quascirev.2011.09.001

Elder, W. P. (1988). Geometry of Upper Cretaceous bentonite beds: implications about volcanic source areas and paleowind patterns, western interior, United States. *Geology*, 16(9), 835–838. https://doi.org/10.1130/0091-7613(1988)016<0835:GOUCBB>2.3.CO;2

Di Fiori, R. V., Long, S. P., Fetrow, A. C., Snell, K. E., Bonde, J. W., & Vervoort, J. D. (2020). Syn-Contractional Deposition of the Cretaceous Newark Canyon Formation, Diamond Mountains, Nevada: Implications for Strain Partitioning Within the North American Cordillera. *Geosphere*, 16, 1–21. https://doi.org/10.1130/abs/2019am-335173

Di Fiori, R. V, Long, S. P., Fetrow, A. C., Snell, K. E., Bonde, J. W., & Vervoort, J. D. (2021). The Role of Shortening in the Sevier Hinterland Within the U. S. Cordilleran Retroarc Thrust System: Insights from the Cretaceous Newark Canyon Formation in Central Nevada. *Tectonics*, 40, 1–31. https://doi.org/10.1029/2020TC006331

Fetrow, A. C., Snell, K. E., DI Fiori, R. V, Long, S. P., & Bonde, J. W. (2020). Early Sevier Orogenic Deformation Exerted Principal Control on Changes in Depositional Environment Recorded by the Cretaceous Newark Canyon Formation. *Journal of Sedimentary Research*, 90(September), 1–22. https://doi.org/10.2110/jsr.2020.52

Flugel, E. (2004). Microfacies of carbonate rocks: Analysis, Interpretation and Application (2nd ed.). Springer International Publishing. https://doi.org/10.1007/10.1007/978-3-642-03796-2

Fluteau, F., Ramstein, G., Besse, J., Guiraud, R., & Masse, J. P. (2007). Impacts of palaeogeography and sea level changes on Mid-Cretaceous climate. *Palaeogeography, Palaeoclimatology, Palaeoecology*, 247(3–4), 357–381. https://doi.org/10.1016/j.palaeo.2006.11.016

Folk, R. L. (1959). Practical Petrographic Classification of Limestones. *Bulletin of the American Association of Petroleum Geologists*, 43(1), 1–38. https://doi.org/10.1306/0BDA5C36-16BD-11D7-8645000102C1865D

Folk, R. L. (1962). Spectral Subdivision of Limestone Types. Proceedings of the Symposium of the Association and the Society of Economic Paleontologists and Mineralogists. Denver, CO. April 12, 1961.

Föllmi, K. B. (2012). Early Cretaceous life, climate, and anoxia. *Cretaceous Research*, 35(C), 230–257. https://doi.org/10.1016/j.cretres.2011.12.005

Forster, A., Schouten, S., Baas, M., & Sinninghe Damsté, J. S. (2007). Mid-Cretaceous (Albian-Santonian) sea surface temperature record of the tropical Atlantic Ocean. *Geology*, 35(10), 919–922. https://doi.org/10.1130/G23874A.1

Fouch, T. D., Hanley, J. H., & Forester, R. M. (1979). Preliminary Correlation of Cretaceous and Paleogene Lacustrine and Related Nonmarine Sedimentary and Volcanic Rocks in Parts of the Eastern Great Basin of Nevada and Utah. In G. W. Newman & H. D. Goode (Eds*.), Basin and Range Symposium and Great Basin field conference* (pp. 305–3012). Rocky

Mountain Association of Petroleum Geologists and Utah Geological Association. http://archives.datapages.com/data/rmag/BasRanSym79/fouch.pdf

Frakes, L. A., & Francis, J. E. (1988). A guide to Phanerozoic cold polar climates from high-latitude ice-rafting in the Cretaceous. *Nature*, 333(9), 547–549. https://doi.org/10.1038/333547a0

Freytet, P., & Verrecchia, E. P. (2002). Lacustrine and palustrine carbonate petrography: an overview. Journal of Paleolimnology, 27, 221–237. https://doi.org/10.1023/A:1014263722766

Fricke, H. C., & O'Neil, J. R. (1999). The correlation between 18O/16O ratios of meteoric water and surface temperature its use in investigating terres. *Earth and Planetary Science Letters*, *170*, 181–196.

Gale, A. (2000). The Cretaceous World. In P. F. Culver, S.J., Rawson (Ed.), *Biotic Response to Global Change. The Last 145 Million Years* (pp. 4–19). Cambridge: Cambridge University Press. https://doi.org/10.1669/0883-1351(2004)019<0618:br>2.0.co;2

Gallagher, T. M., & Sheldon, N. D. (2016). Combining soil water balance and clumped isotopes to understand the nature and timing of pedogenic carbonate formation. *Chemical Geology*, *435*. https://doi.org/10.1016/j.chemgeo.2016.04.023

Ghosh, P., Garzione, C. N., & Eiler, J. M. (2006). Rapid Uplift of the Altiplano Revealed Through 13C-18O Bonds in Paleosol Carbonates. *Science*, 311(5760), 511–515. http://www.sciencemag.org/cgi/doi/10.1126/science.1119365

Gierlowski-Kordesch, E. H. (2010). Lacustrine Carbonates. *In Developments in Sedimentology* (Vol. 61, pp. 1–101). Elsevier. https://doi.org/10.1016/S0070-4571(09)06101-9

Goldberg, S. L., Present, T. M., Finnegan, S., & Bergmann, K. D. (2021). A high-resolution record of early Paleozoic climate. *Proceedings of the National Academy of Sciences of the United States of America*, 118(6). https://doi.org/10.1073/pnas.2013083118

Gonfiantini, R., Wassenaar, L. I., Araguas-Araguas, L., & Aggarwal, P. K. (2018). A unified Craig-Gordon isotope model of stable hydrogen and oxygen isotope fractionation during fresh or saltwater evaporation. *Geochimica et Cosmochimica Acta*, 235, 224–236. https://doi.org/10.1016/j.gca.2018.05.020

Gray, M. B., & Nickelsen, R. P. (1989). Pedogenic slickensides, indicators of strain and deformation processes in redbed sequences of the Appalachian foreland. *Geology*, 17(1), 72–75. https://doi.org/10.1130/0091-7613(1989)017<0072:PSIOSA>2.3.CO;2

Gröcke, D. R., Hesselbo, S. P., & Jenkyns, H. C. (1999). Carbon-isotope composition of Lower Cretaceous fossil wood: Ocean-atmosphere chemistry and relation to sea-level change. *Geology*, 27(2), 155–158. https://doi.org/10.1130/0091-7613(1999)027<0155:CICOLC>2.3.CO;2

Harbeck, G. E. (1962). A practical Field Technique For Measuring Reservoir Evaporation utilizing Mass-Transfer Theory. *US Geological Survey Professional Paper,* 272-E, 101–105. http://pubs.usgs.gov/pp/0272e/report.pdf

Hasegawa, H., Tada, R., Jiang, X., Suganuma, Y., Imsamut, S., Charusiri, P., Ichinnorov, N., and Khand, Y. (2012). Drastic shrinking of the Hadley circulation during the mid-Cretaceous Supergreenhouse. *Climate of the Past*, 8(4), 1323–1337. https://doi.org/10.5194/cp-8-1323-2012

Hay, W. W., DeConto, R. M., de Boer, P., Flögel, S., Song, Y., & Stepashko, A. (2018). Possible solutions to several enigmas of Cretaceous climate. *International Journal of Earth Science*s (Vol. 108). Springer Berlin Heidelberg. https://doi.org/10.1007/s00531-018-1670-2

Held, I. M., & Soden, B. J. (2002). Water Vapor Feedback and Global Warming. *Annual Review of Energy and the Environment*, 25(1), 441–475. https://doi.org/10.1146/annurev.energy.25.1.441

Held, I. M., & Soden, B. J. (2006). Robust responses of the hydrological cycle to global warming. *Journal of Climate*, 19, 5686–5699. https://doi.org/10.1175/JCLI3990.1

Henkes, G. A., Passey, B. H., Grossman, E. L., Yancey, T. E., Shenton, B. J., Pe, A., Pérez-Huerta, A., and Yancey, T. E. (2014). Temperature limits for preservation of primary calcite clumped isotope paleotemperatures. *Geochimica et Cosmochimica Acta*, 139, 362–382. https://doi.org/10.1016/j.gca.2014.04.040

Hough, B. G., Fan, M., & Passey, B. H. (2014). Calibration of the clumped isotope geothermometer in soil carbonate in Wyoming and Nebraska, USA: Implications for paleoelevation and paleoclimate reconstruction. *Earth and Planetary Science Letters*, *391*(C), 110–120. https://doi.org/10.1016/j.epsl.2014.01.008

Huber, B. T., MacLeod, K. G., Watkins, D. K., & Coffin, M. F. (2018). The rise and fall of the Cretaceous Hot Greenhouse climate. *Global and Planetary Change*, 167, 1–23. https://doi.org/10.1016/j.gloplacha.2018.04.004

Huber, B. T., Hodell, D. A., & Hamilton, C. P. (1995). Middle-late Cretaceous climate of the southern high latitudes: stable isotopic evidence for minimal equator-to-pole thermal gradients. *Geological Society of America Bulletin*, 107(10), 1164–1191. https://doi.org/10.1130/0016-7606(1995)107<1164:MLCCOT>2.3.CO;2

Huber, B. T., Norris, R. D., & MacLeod, K. G. (2002). Deep-sea paleotemperature record of extreme warmth during the Cretaceous. *Geology*, 30(2), 123–126. https://doi.org/10.1130/0091-7613(2002)030<0123:DSPROE>2.0.CO;2

Huber, M. (2008). A hotter greenhouse? *Science*, 321(5887), 353–354.2008

Huntington, K. W., Eiler, J. M., Affek, H. P., Guo, W., Bonifacie, M., Yeung, L. Y., Thiagarajan, N., Passey, B., Tripati, A., Daëron, M., and Came, R (2009). Methods and limitations of 'clumped' CO_2 isotope (Δ_{47}) analysis by gas-source isotope ratio mass spectrometry. *Journal of Mass Spectrometry*, 44(9), 1318–1329. http://doi.wiley.com/10.1002/jms.1614

Huntington, K. W., Wernicke, B. P., & Eiler, J. M. (2010). Influence of climate change and uplift on Colorado Plateau paleotemperatures from carbonate clumped isotope thermometry. *Tectonics*. http://onlinelibrary.wiley.com/doi/10.1029/2009TC002449/full

Ingalls, M., Frantz, C. M., Snell, K. E., & Trower, E. J. (2020). Carbonate facies-specific stable isotope data record climate, hydrology, and microbial communities in Great Salt Lake, UT. *Geobiology*, *18*(5), 566–593. https://doi.org/10.1111/gbi.12386

Ingalls, M., Fetrow, A. C., Snell, K. E., Frantz, C. M., & Trower, E. J. (2022). Lake level controls the recurrence of giant stromatolite facies. *Sedimentology*, 1–26. https://doi.org/10.1111/sed.12967

Jenkyns, H. C. (2010). Geochemistry of oceanic anoxic events. *Geochemistry, Geophysics, Geosystems*, 11(3), 1–30. https://doi.org/10.1029/2009GC002788

Jordan, T. E., & Allmendinger, R. W. (1986). The Sierra Pampeanas of Argentina: A Modern Analogue of Rocky Mountain Foreland Deformation. *American Journal of Science*, *286*, 737–764. https://doi.org/10.2475/ajs.286.10.737

Jouzel, J., Alley, R. B., Cuffey, K. M., Dansgaard, W., Grootes, P., Hoffmann, G., Johnsen, S. J., Koster, R. D., Peel, D., Shuman, C. A., Stievenard, M., Stuiver, M., and White, J. (1997). Validity of the temperature reconstruction from water isotopes in ice cores. *Journal of Geophysical Research: Oceans*, 102(C12), 26471–26487. https://doi.org/10.1029/97JC01283

Kelson, J. R., Huntington, K. W., Breecker, D. O., Burgener, L. K., Gallagher, T. M., Hoke, G. D., & Petersen, S. V. (2020). A proxy for all seasons? A synthesis of clumped isotope data from Holocene soil carbonates. *Quaternary Science Reviews*, *234*(106259), 1–18. https://doi.org/10.1016/j.quascirev.2020.106259

Kim, S.-T., & O'Neil, J. R. (1997). Equilibrium and nonequilibrium oxygen isotope effects in synthetic carbonates. *Geochimica et Cosmochimica Acta*, 61(16), 3461–3475. https://doi.org/10.1016/S0016-7037(97)00169-5

Kopf, S., Davidheiser-Kroll, B., & Kocken, I. (2021). Isoreader: An R package to read stable isotope data files for reproducible research. *Journal of Open Source Software*, 6(61), 2878. https://doi.org/10.21105/joss.02878

Kraus, M. J. (1999). Paleosols in clastic sedimentary rocks: Their geologic applications. *Earth Science Reviews*, 47(1–2), 41–70. https://doi.org/10.1016/S0012-8252(99)00026-4

Leng, M. J., & Marshall, J. D. (2004). Palaeoclimate interpretation of stable isotope data from lake sediment archives. *Quaternary Science Reviews*, *23*(7–8), 811–831. Retrieved from http://linkinghub.elsevier.com/retrieve/pii/S0277379104000101

Li, H. C., & Ku, T. L. (1997). ^{13}C- ^{18}O covariance as a paleohydrological indicator for closed-basin lakes. *Palaeogeography, Palaeoclimatology, Palaeoecology*, 133(1–2), 69–80. https://doi.org/10.1016/S0031-0182(96)00153-8

Long, S.P. (2012) Magnitudes and spatial patterns of erosional exhumation in the Sevier hinterland, eastern Nevada and western Utah, USA: Insights from a Paleogene paleogeologic map: Geosphere, v. 8, p. 881-901, doi:10.1130/GES00783.1.

Long, S. P. (2015). An upper-crustal fold province in the hinterland of the Sevier orogenic belt, eastern Nevada, U.S.A.: A Cordilleran Valley and Ridge in the Basin and Range. *Geosphere*, 11(2), 404–424. http://geosphere.gsapubs.org/content/11/2/404.full

Long, S. P. (2019). Geometry and extension magnitude of the Basin and Range Province (39°N), Utah, Nevada, and California, USA: Constraints from a province-scale cross section. *Geological Society of America Bulletin*, 1–21. https://doi.org/10.1130/B31974.1

Long, S. P., Henry, C. D., Muntean, J. L., Edmondo, G. P., & Cassel, E. J. (2014). Early Cretaceous construction of a structural culmination, Eureka, Nevada, U.S.A.: Implications for out-of-sequence deformation in the Sevier hinterland. *Geosphere*, 10(3), 564–584. https://doi.org/10.1130/GES00997.1

Long, S. P., Thomson, S. N., Reiners, P. W., & Di Fiori, R. V. (2015). Synorogenic extension localized by upper-crustal thickening: An example from the Late Cretaceous Nevadaplano. *Geology*, 43(4), 351–354. https://doi.org/10.1130/G36431.1

Long, S. P., & Soignard, E. (2016). Shallow-crustal metamorphism during Late Cretaceous anatexis in the Sevier hinterland plateau: Peak temperature conditions from the Grant Range, eastern Nevada, U.S.A. *Lithosphere*, 8(2), 150–164. http://lithosphere.gsapubs.org/lookup/doi/10.1130/L501.1

Long, S. P., Henry, C. D., Muntean, J. L., Edmondo, G. P., & Thomas, R. D. (2014). Preliminary geologic map of the southern Eureka Mining District, Eureka and White Pine counties, Nevada. Plate 1 of 2. Nevada Bureau of Mines and Geology, *Nevada Geological Survey*, 1. http://publication/uuid/FE87EC43-D223-4AAF-9618-1FE7F4F836DE

Ludvigson, G. A., Joeckel, R. M., Murphy, L. R., Stockli, D. F., González, L. A., Suarez, C. A., Kirkland, J. I., Al-Suwaidi, A. H. (2015). The emerging terrestrial record of Aptian-Albian global change. *Cretaceous Research*, 56, 1–24. https://doi.org/10.1016/j.cretres.2014.11.008

Ludvigson, G. A., Joeckel, R. M., Gonzalez, L. A., Gulbranson, E. L., Rasbury, E. T., Hunt, G. J., Kirkland, J. I., Madsen, S. (2010). Correlation of Aptian-Albian carbon isotope excursions in continental strata of the cretaceous Foreland Basin, Eastern Utah, U.S.A. *Journal of Sedimentary Research*, 80(11–12), 955–974. https://doi.org/10.2110/jsr.2010.086

Luz, B., Barkan, E., Yam, R., & Shemesh, A. (2009). Fractionation of oxygen and hydrogen isotopes in evaporating water. *Geochimica et Cosmochimica Acta*, 73(22), 6697–6703. https://doi.org/10.1016/j.gca.2009.08.008

Mack, G. H., James, W. C., & Monger, H. C. (1993). Classification of paleosols. *Geological Society of America Bulletin*, 105(2), 129–136. https://doi.org/10.1130/0016-7606(1993)105<0129:COP>2.3.CO;2

MacNeil, F. S. (1939). Fresh-Water Invertebrates and Land Plants of Cretaceous Age from Eureka Nevada. *Journal of Paleontology*, 13(3), 355–360. https://www.jstor.org/stable/1298743

Makaske, B. (2001). Anastomosing rivers: A review of their classification, origin and sedimentary products. *Earth Science Reviews*, 53, 149–196. https://doi.org/10.1016/S0012-8252(00)00038-6

Martin-Bello, L., Arenas, C., Andrews, J. E., Alonso-Zarza, A. M., & Marca, A. (2019). Lacustrine stromatolites as multi-scale recorders of climate change: Insights from the Miocene Ebro Basin. *Palaeogeography, Palaeoclimatology, Palaeoecology*, 530(September 2018), 312–329. https://doi.org/10.1016/j.palaeo.2019.05.001

Marty, D., & Meyer, C. A. (2006). Depositional conditions of carbonate-dominated palustrine sedimentation around the K-T boundary (Faciès Rognacien, northeastern Pyrenean foreland, southwestern France). In A. M. Alonso-Zarza & L. H. Tanner (Eds.), *Paleoenvironmental Record and Applications of Calcretes and Palustrine Carbonates* (Special Pa, Vol. 416, pp. 169–187). Geological Society of America. https://doi.org/10.1130/SPE416

McDonough, K. J., & Cross, T. A. (1991). Late Cretaceous sea level from a paleoshoreline. *Journal of Geophysical Research*, 96(B4), 6591–6607. https://doi.org/10.1029/91JB00281

Mildrexler, D. J., Zhao, M., & Running, S. W. (2011). Satellite finds highest land skin temperatures on Earth. *Bulletin of the American Meteorological Society*, 92(7), 855–860. https://doi.org/10.1175/2011BAMS3067.1

Miller, K. G., Sciences, G., Herna, J. C., Olsson, R. K., Wright, J. D., & Feigenson, M. D. (2003). Late Cretaceous chronology of large, rapid sea-level changes : Glacioeustasy during the greenhouse world. *Geology*, (7), 585–588. https://doi.org/10.1130/0091-7613(2003)031<0585:LCCOLR>2.0.CO;2

Mintz, J. S., Driese, S. G., Breecker, D. O., & Ludvigson, G. A. (2011). Influence of Changing Hydrology on Pedogenic Calcite Precipitation in Vertisols, Dance Bayou, Brazoria County, Texas, U.S.A.: Implications for Estimating Paleoatmospheric pCO_2. *Journal of Sedimentary Research*, 81(6), 394–400. http://jsedres.sepmonline.org/cgi/doi/10.2110/jsr.2011.36

Murru, M., Ferrara, C., & Matteucci, R. (2015). Paleocene palustrine and ephemeral alluvial facies in southern Sardinia (Italy). *Italian Journal of Geosciences*, 134(1), 134–148. https://doi.org/10.3301/IJG.2014.32

Nadon, G. C. (1994). The Genesis and Recognition of Anastomosed Fluvial Deposits: Data from the St. Mary River Formation, Southwestern Alberta, Canada. *Journal of Sedimentary Research*, B64(4), 451–463. https://doi.org/10.1306/D4267FE1-2B26-11D7-8648000102C1865D

Nolan, T. B., Merriam, C. W., & Blake, M. C. J. (1974). Geologic Map of Pinto Summit Quadrangle, Eureka and White Pine Counties, Nevada: *U.S. Geological Survey Miscellaneous Investigations* Series Map I-793.

Nolan, T. B., & Hunt, R. N. (1962). The Eureka Mining District Nevada. https://doi.org/10.3133/pp406

Nolan, T. B., Merriam, C. W., & Williams, J. S. (1956). The stratigraphic section in the vicinity of Eureka, Nevada. *Geological Survey Professional Paper* (Vol. 276). https://doi.org/10.3133/pp276

Olivero, E. B., Gasparini, Z., Rinaldi, C. A., & Scasso, R. A. (1991). First record of dinosaurs in Antarctica (Upper Cretaceous, James Ross Island): palaeogeographical implications. In M. R. A. Thomson, J. A. Crame, & J. W. Thomson (Eds.), *Geological Evolution of Antarctica* (pp. 617–622). London: Cambridge University Press.

Pagani, M., Huber, M., & Sageman, B. (2013). Greenhouse Climates. In *Treatise on Geochemistry* (2nd ed., Vol. 6, pp. 281–304). Elsevier Ltd. https://doi.org/10.1016/B978-0-08-095975-7.01314-0

Pagel, M., Barbin, V., Blanc, P., & Ohnenstetter, D. (2000). Cathodoluminescence in Geosciences. (M. Pagel, V. Barbin, P. Blanc, & D. Ohnenstetter, Eds.). Springer-Verlag.

Parrish, J. M., Parrish, J. T., Hutchison, J. H., & Spicer, R. A. (1987). Late Cretaceous Vertebrate Fossils from the North Slope of Alaska and Implications for Dinosaur Ecology. *PALAIOS*, 2(4), 377–389.

Parrish, J. T., & Spicer, R. A. (1988). Late Cretaceous terrestrial vegetation: A near-polar temperature curve. *Geology*, 16(1), 22–25. https://doi.org/10.1130/0091-7613(1988)016<0022:LCTVAN>2.3.CO;2

Passey, B. H., Levin, N. E., Cerling, T. E., Brown, F. H., & Eiler, J. M. (2010). High-temperature environments of human evolution in East Africa based on bond ordering in paleosol carbonates. In *Proceedings of the National Academy of Sciences*. http://www.pnas.org/content/107/25/11245.short

Passey, B. H., & Henkes, G. A. (2012). Carbonate clumped isotope bond reordering and geospeedometry. *Earth and Planetary Science Letters*, 351–352, 223–236. https://doi.org/10.1016/j.epsl.2012.07.021

Petersen, S. V., Defliese, W. F., Saenger, C., Daëron, M., Huntington, K. W., John, C. M., Kelson, J. R., Bernasconi, S. M., Colman, A. S., Kluge, T., Olack, G. A., Schauer, A. J., Bajnai, D., Bonifacie, M., Breitenbach, S. F., Fiebig, J., Fernandez, A., Henkes, G. A., Hodell, D. A., Katz, A., Winkelstern, I. Z., Kele, S., Lohmann, K.C., Passey, B. H., Petrizzo, D. A., Rosenheim, B. E., Tripati, A. K., Venturelli, R., Young, E. D., and Wacker, U. (2019). Effects of Improved ^{17}O Correction on Inter-Laboratory Agreement in Clumped Isotope Calibrations, Estimates of Mineral-Specific Offsets, and Acid Fractionation Factors. *Geochemistry, Geophysics, Geosystems*. https://doi.org/10.1029/2018GC008127

Platt, N. H. (1989). Lacustrine carbonates and pedogenesis: sedimentology and origin of palustrine deposits from the Early Cretaceous Rupelo Formation, W. Cameros Basin, N Spain. *Sedimentology*, 36(4), 665–684. https://doi.org/10.1111/j.1365-3091.1989.tb02092.x

Poulsen, C. J., Barron, E. J., Johnson, C. C., & Fawcett, P. (1999). Links between major climatic factors and regional oceanic circulation in the mid-Cretaceous. *Geological Society Special Publication*, Evolution (Special Paper 332).

Poulsen, C. J., Barron, E. J., Arthur, M. A., & Peterson, W. H. (2001). Response of the mid-Cretaceous global oceanic circulation to tectonic and CO_2 forcings. *Paleoceanography*, 16(6), 576–592. https://doi.org/10.1029/2000PA000579

Poulsen, C. J., & Jeffery, M. L. (2011). Climate change imprinting on stable isotopic compositions of high-elevation meteoric water cloaks past surface elevations of major orogens. *Geology*. http://geology.gsapubs.org/content/39/6/595.short

Qiao, D., Peng, N., Kuang, H., Liu, Y., Liu, Y., Cui, L., & Wang, Y. (2022). Changes in prevailing surface-paleowinds reveal the atmospheric circulation transition during Early Cretaceous in North China. *Palaeogeography, Palaeoclimatology, Palaeoecology*, 586(November 2021), 110784. https://doi.org/10.1016/j.palaeo.2021.110784

Quade, J., Eiler, J., Daëron, M., & Achyuthan, H. (2013). The clumped isotope geothermometer in soil and paleosol carbonate. *Geochimica et Cosmochimica Acta*, 105, 92–107. http://dx.doi.org/10.1016/j.gca.2012.11.031

Rich, P. V., Rich, T. H., Wagstaff, B. E., Mason, J. M. E., Douthitt, C. B., Gregory, R. T., & Felton, E. A. (1988). Evidence for low temperatures and biologic diversity in cretaceous high latitudes of Australia. *Science*, 242(4884), 1403–1406. https://doi.org/10.1126/science.242.4884.1403

Rich, T. H., Vickers-rich, P., & Gangloff, R. A. (2002). Polar Dinosaurs. *Science*, 295(5557), 979–981. https://doi.org/10.1126/science.1068920

Rozanski, K., Araguás Araguás, L., & Gonfiantini, R. (1993). *Isotopic Patterns in Modern Global Precipitation. Climate Change in Continental Isotopic Records* (Vol. 78). Washington, D. C.: American Geophysical Union. http://www.agu.org/books/gm/v078/GM078p0001/GM078p0001.shtml

Ryb, U., Lloyd, M. K., & Eiler, J. M. (2021). Carbonate clumped isotope constraints on burial, uplift and exhumation histories of the Colorado Plateau.

Earth and Planetary Science Letters, *566*, 116964. https://doi.org/10.1016/j.epsl.2021.116964

Schauble, E. A., Ghosh, P., & Eiler, J. M. (2006). Preferential formation of 13C-18O bonds in carbonate minerals, estimated using first-principles lattice dynamics. *Geochimica et Cosmochimica Acta*, 70(10), 2510–2529. https://doi.org/10.1016/j.gca.2006.02.011

Scott, R. W., Oboh-Ikuenobe, F. E., Benson, D. G., Holbrook, J. M., & Alnahwi, A. (2018). Cenomanian-Turonian flooding cycles: U.S. Gulf Coast and Western Interior. *Cretaceous Research*, *89*, 191–210. https://doi.org/10.1016/j.cretres.2018.03.027

Secord, R., Gingerich, P. D., Lohmann, K. C., & MacLeod, K. G. (2010). Continental warming preceding the Palaeocene-Eocene thermal maximum. *Nature*, 467(7318), 955–958. https://doi.org/10.1038/nature09441

Smith, J. K., & Ketner, K. B. (1976). Stratigraphy of post-Paleozoic rocks and summary of resources in the Carlin-Pinon Range area, Nevada, with a section on aeromagnetic survey. *Geological Survey Professional Paper*. https://doi.org/10.3133/pp867B

Snell, K. E., Thrasher, B. L., Eiler, J. M., Koch, P. L., Sloan, L. C., & Tabor, N. J. (2013). Hot summers in the Bighorn Basin during the early Paleogene. *Geology*, 41(1), 55–58. https://doi.org/10.1130/G33567.1

Strawson, F. M. (1981). The geology of the Permian Carbon Ridge Formation, East-Central Nevada. University of Nevada Reno. https://scholarworks.unr.edu/handle/11714/1732

Suarez, C. A., González, L. A., Ludvigson, G. A., Kirkland, J. I., Cifelli, R. L., & Kohn, M. J. (2014). Multi-taxa isotopic investigation of paleohydrology in the lower cretaceous cedar mountain formation, Eastern Utah, U.S.A.: Deciphering effects of the Nevadaplano plateau on regional climate. *Journal of Sedimentary Research*, 84(11), 975–987. https://doi.org/10.2110/jsr.2014.76

Suarez, M. B., Knight, J. A., Godet, A., Ludvigson, G. A., Snell, K. E., Murphy, L., & Kirkland, J. I. (2021). Multiproxy strategy for determining paleoclimate parameters in the ruby ranch member of the cedar mountain formation. *Geological Society Special Publication*, 507(1), 313–334. https://doi.org/10.1144/SP507-2020-85

Suarez, M. B., González, L. A., & Ludvigson, G. A. (2011). Quantification of a greenhouse hydrologic cycle from equatorial to polar latitudes: The mid-Cretaceous water bearer revisited. *Palaeogeography, Palaeoclimatology, Palaeoecology*, 307(1–4), 301–312. https://doi.org/10.1016/j.palaeo.2011.05.027

Takashima, R., Nishi, H., Huber, B. T., & Leckie, R. M. (2006). Greenhouse World and the Mesozoic Ocean. *Oceanography*, 19(4), 64–74. https://doi.org/10.5670/oceanog.2006.07

Talbot, M. R. (1990). A review of the palaeohydrological interpretation of carbon and oxygen isotopic ratios in primary lacustrine carbonates. *Chemical Geology*: Isotope Geoscience Section, 80(4), 261–279. https://doi.org/10.1016/0168-9622(90)90009-2

Tarduno, J. A., Brinkman, D. B., Renne, P. R., Cottrell, R. D., Scher, H., & Castillo, P. (1998). Evidence for extreme climatic warmth from late cretaceous arctic vertebrates. *Science*, 282(5397), 2241–2244. https://doi.org/10.1126/science.282.5397.2241

Tucker, M. E., & Wright, V. P. (1990). Carbonate Sedimentology. Blackwell Publishing Ltd. https://doi.org/10.1002/9781444314175

Ufnar, D. F., Ludvigson, G. A., González, L., & Gröcke, D. R. (2008). Precipitation rates and atmospheric heat transport during the Cenomanian greenhouse warming in North America: Estimates from a stable isotope mass-balance model. *Palaeogeography, Palaeoclimatology, Palaeoecology*, 266(1–2), 28–38. https://doi.org/10.1016/j.palaeo.2008.03.033

Ufnar, D. F., González, L. A., Ludvigson, G. A., Brenner, R. L., & Witzke, B. J. (2002). The mid-cretaceous water bearer: Isotope mass balance quantification of the Albian hydrologic cycle. *Palaeogeography, Palaeoclimatology, Palaeoecology*, 188(1–2), 51–71. https://doi.org/10.1016/S0031-0182(02)00530-8

Ufnar, D. F., González, L. A., Ludvigson, G. A., Brenner, R. L., & Witzke, B. J. (2004). Evidence for increased latent heat transport during the Cretaceous (Albian) greenhouse warming. *Geology*, 32(12), 1049–1052. https://doi.org/10.1130/G20828.1

Vandervoort, D. S. (1987). Sedimentology, Provenance, and Tectonic Implications of the Cretaceous Newark Canyon Formation. Montana State University. https://scholar.googleusercontent.com/scholar?q=cache:dedPFxQl5mwJ:scholar.google.com/+Sedimentology,-

Vandervoort, D. S., & Schmitt, J. G. (1990). Cretaceous to early Tertiary paleogeography in the hinterland of the Sevier thrust belt, east-central Nevada. *Geology*, 18, 567–570. https://doi.org/10.1130/0091-7613(1990)018<0567:CTETPI>2.3.CO;2

Voigt, S., Gale, A. S., & Voigt, T. (2006). Sea-level change, carbon cycling and paleoclimate during the Late Cenomanian of northwest Europe; an integrated paleoenvironmental analysis. *Cretaceous Research*, 27(6), 836–858. https://doi.org/10.1016/j.cretres.2006.04.005

Wells, M. L., Hoisch, T. D., Cruz-Uribe, A. M., & Vervoort, J. D. (2012). Geodynamics of synconvergent extension and tectonic mode switching: Constraints from the Sevier-Laramide orogen. *Tectonics*, 31(1), 1–20. https://doi.org/10.1029/2011TC002913

Wendler, J. E., & Wendler, I. (2016). What drove sea-level fluctuations during the mid-Cretaceous greenhouse climate? *Palaeogeography, Palaeoclimatology, Palaeoecology*, 441, 412–419. http://dx.doi.org/10.1016/j.palaeo.2015.08.029

White, T., González, L., Ludvigson, G., & Poulsen, C. (2001). Middle Cretaceous greenhouse hydrologic cycle of North America. *Geology*, 29(4), 363–366. https://doi.org/10.1130/0091-7613(2001)029<0363:MCGHCO>2.0.CO;2

Wright, V. P., & Peeters, C. (1989). Origins of some Early Carboniferous calcrete fabrics revealed by cathodoluminescence: implications for interpreting the sites of calcrete formation. *Sedimentary Geology*, 65, 345–353. https://doi.org/10.1016/0037-0738(89)90033-X

Wright, V. P., & Platt, N. H. (1995). Seasonal wetland carbonate sequences and dynamic catenas: a re-appraisal of palustrine limestones. *Sedimentary Geology*, 99, 65–71. https://doi.org/10.1016/0037-0738(95)00080-R

Yonkee, W. A., & Weil, A. B. (2015). Tectonic evolution of the Sevier and Laramide belts within the North American Cordillera orogenic system. *Earth-Science Reviews*, 150, 531–593. https://doi.org/10.1016/j.earscirev.2015.08.001

Zamanian, K., Pustovoytov, K., & Kuzyakov, Y. (2016). Pedogenic carbonates: Forms and formation processes. *Earth-Science Reviews*, *157*, 1–17. https://doi.org/10.1016/j.earscirev.2016.03.003

Zuza, A. V., Levy, D. A., Mulligan, S., Zuzu, A. V, Levy, D. A., & Mulligan, S. (2020). Geologic field evidence for non-lithostatic overpressure recorded in the North American Cordillera hinterland, northeast Nevada. *Geosciences Frontier*, 95(14), 106408. https://doi.org/10.1016/j.gsf.2020.10.006